Biophysical *Journal*
Computational Tool

Biophysical Society

A Preferred Curvature-Based Continuum Mechanics Framework for Modeling Embryogenesis

Khaled Khairy,[1,*] William Lemon,[1] Fernando Amat,[1] and Philipp J. Keller[1,*]
[1]Howard Hughes Medical Institute, Ashburn, Virginia

ABSTRACT Mechanics plays a key role in the development of higher organisms. However, understanding this relationship is complicated by the difficulty of modeling the link between local forces generated at the subcellular level and deformations observed at the tissue and whole-embryo levels. Here we propose an approach first developed for lipid bilayers and cell membranes, in which force-generation by cytoskeletal elements enters a continuum mechanics formulation for the full system in the form of local changes in preferred curvature. This allows us to express and solve the system using only tissue strains. Locations of preferred curvature are simply related to products of gene expression. A solution, in that context, means relaxing the system's mechanical energy to yield global morphogenetic predictions that accommodate a tendency toward the local preferred curvature, without a need to explicitly model force-generation mechanisms at the molecular level. Our computational framework, which we call SPHARM-MECH, extends a 3D spherical harmonics parameterization known as SPHARM to combine this level of abstraction with a sparse shape representation. The integration of these two principles allows computer simulations to be performed in three dimensions on highly complex shapes, gene expression patterns, and mechanical constraints. We demonstrate our approach by modeling mesoderm invagination in the fruit-fly embryo, where local forces generated by the acto-myosin meshwork in the region of the future mesoderm lead to formation of a ventral tissue fold. The process is accompanied by substantial changes in cell shape and long-range cell movements. Applying SPHARM-MECH to whole-embryo live imaging data acquired with light-sheet microscopy reveals significant correlation between calculated and observed tissue movements. Our analysis predicts the observed cell shape anisotropy on the ventral side of the embryo and suggests an active mechanical role of mesoderm invagination in supporting the onset of germ-band extension.

INTRODUCTION

Embryonic development is accompanied by fundamental changes in shape, including long-range tissue reorganization and epithelial folding. At the cellular and molecular levels, these morphogenetic processes are driven by cytoskeletal reorganization, leading to force generation (1–6). This activity is orchestrated at the whole-embryo level through differential expression of genes. In addition, mechanical constraints also determine and limit morphological configurations available to a developing organism, and the forces generated in turn influence gene expression itself (7–9). It is thought that forces are transmitted over long ranges through the material of a tissue. However, details of how forces exercise such long-range effects can only be understood by combining experimental data and computational models. With advances in microscopy technology, detailed live imaging data of whole-embryo morphogenesis have become available (10–12) (Fig. 1 *a*; Movies S1 and S2). Large-scale approaches to imaging and computational image analysis have produced near-comprehensive quantitative gene expression distribution maps for the early embryo (13,14) (Fig. 1 *b*). Therefore, it should be possible to predict observed tissue movements and cell shape changes that result from local force generation, by considering whole-embryo tissue mechanics.

There have been a number of efforts to model morphogenesis on the computer (15,16), for example, in the fruit fly (17–24), the sea urchin (25,26), and the chick embryo (27,28). However, accurate 3D modeling of embryogenesis remains a difficult task. A major challenge is the requirement of a multidimensional mathematical representation that is able to express embryo shape, gene expression patterns, and material properties accurately, and in a manner that allows efficient numerical application of constitutive tissue behavior. A second challenge is to link force-generating mechanisms, which occur at the subcellular level through

Submitted July 12, 2017, and accepted for publication November 14, 2017.
*Correspondence: khairyk@janelia.hhmi.org or kellerp@janelia.hhmi.org
William Lemon and Fernando Amat contributed equally to this work.
Editor: Stanislav Shvartsman.
https://doi.org/10.1016/j.bpj.2017.11.015

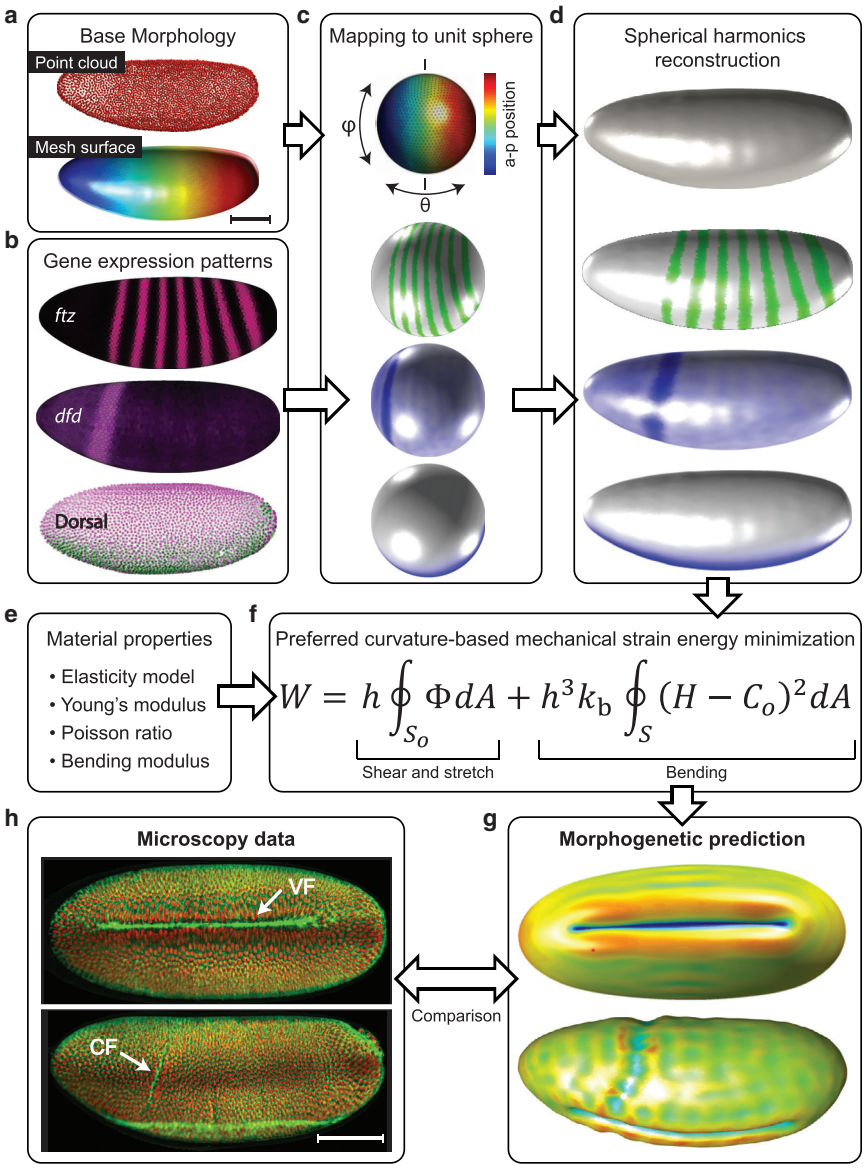

FIGURE 1 SPHARM-MECH overview. (*a*) Morphology data is shown. (*Top*) Given here are cell centers from segmentation of the nuclear label His2Av-RFP channel from a 3D stack of a live adaptive SiMView light-sheet microscopy recording of a whole *D. melanogaster* embryo at the cellularized blastoderm stage. (*Bottom*) Surface triangular mesh is based on cell centers. Color-code anterior-posterior (*y* axis) with color bar is as in the top of (*c*). (*b*) Given here is gene expression data, with example gene expression patterns of *ftz*, *dfd*, and *dl*. The *ftz* and *dfd* patterns are displayed using PointCloudXplore (13). (*c*) Given here is spherical mapping. Cartesian coordinates (*top*) color code corresponds to (*a*) bottom with values provided in color bar. Gene expression patterns of *ftz*, *dfd*, and *dl* are mapped onto the unit sphere. (*d*) Given here is a spherical harmonics reconstruction (projection). Based on the spherical mapping in (*c*), Fourier coefficients are calculated for morphology and gene expression patterns to produce the internal analytical representation used by SPHARM-MECH (see Supporting Materials and Methods in the Supporting Material). The outline is represented by 25 numbers (SPHARM coefficients). (*e*) Material properties data may be obtained from experimental measurements or estimated based on physical assumptions. (*f*) Given here is energy minimization. Gene product activity increases the configuration-dependent strain energy by inducing local changes to preferred curvature. Morphology changes occur to relieve that energy (see Supporting Materials and Methods in the Supporting Material). (*g*) Given here are example SPHARM-MECH simulation results showing formation of the ventral furrow invagination (*top*) and simultaneous simulation of ventral and cephalic furrows (*bottom*). (*h*) Given here are ventral and lateral views of maximum intensity projections of 3D stacks of an adaptive SiMView microscopy recording of a whole *D. melanogaster* embryo, homozygous for the membrane label Spider-GFP and the nuclear label His2Av-RFP, 22 min after onset of gastrulation (see Movies S1 and S2 for complete time-lapse recording). The scale bar represents 100 μm (*a* and *h*).

cytoskeletal dynamics, to a continuum mechanics formulation, which is necessary for performing whole-embryo simulations in realistic computation times. This link should provide a level of abstraction that is able to approximate the activities of various cytoskeleton-level mechanisms, and yet communicate their effects on a macroscopic scale in a fashion compatible with standard mechanics treatments.

To address the above challenges, we developed an open-source computational biomechanics framework that we call SPHARM-MECH (Fig. 1). Shape representation is based on a powerful Fourier basis for approximating functions on the sphere known as the spherical harmonics basis functions (Fig. S1 and see the Supporting Material). The spherical harmonics have been used to represent, register, and compare complex morphologies of simply connected objects through an approach known as SPHARM (29–31). SPHARM, although highly accurate and concise, is limited to shapes of genus zero; this class of shapes represents objects that do not have holes or handles, which applies to the fruit-fly embryo and other biological structures. For shapes of higher topological genus, alternative shape representations are needed; for example, a polygonal mesh as is commonly used in finite element analysis. SPHARM-MECH data representation generalizes the SPHARM approach. It concisely encodes, in addition to morphology, gene expression distributions to facilitate data-driven identification of regions of local gene-product activity (Fig. 1, *a–d*; Methods). Its fidelity to experimental data is limited only by the spatial and temporal resolution of the recording device and noise. Harmonic functions of higher order gradually provide more detail, as expected from a converging Fourier series (Fig. S2). Importantly, gene expression patterns are naturally mapped onto

morphologies independent of their source in a straightforward manner (Fig. 1, *b–d*; Fig. S3, *a–g*; and see the Supporting Material). Using these maps, regions of local mechanical activity are generated (Fig. 2 *a*; Fig. S3 *h*).

Given gene activity maps, a starting morphology (Fig. 1 *d*), and material properties (Fig. 1 *e*), SPHARM-MECH calculates a configuration-dependent strain energy for the whole tissue (Fig. 1 *f*; Methods). We propose that the driving force for tissue invagination and epithelial folds manifests itself mechanically as a departure of the preferred tissue curvature from its current curvature at locations of gene product activity. This can occur via a number of different molecular and cellular mechanisms, the details of which do not enter our analysis. Examples would include contraction of an acto-myosin meshwork driving the ventral furrow invagination (VFI) (Fig. 1 *h*) via apical cell constriction (32), or repositioning of adherens junctions responsible for formation of a dorsal fold (33), both observed in the fruit-fly embryo. Abstraction/omission of these details is intentional in our approach in favor of computational feasibility of whole embryo mechanics modeling. The preferred curvature concept provides the necessary link between effects of local biological force-generating mechanisms and a continuum tissue mechanics formulation. When forces are generated locally, the organism is in a high mechanical energy state. Morphological changes occur to relieve this strained tissue configuration (Fig. 1 *f*). SPHARM-MECH predicts a morphology that minimizes mechanical energy (Fig. 1 *g*) by using standard methods of numerical optimization (Methods).

The presented method is an approximation within the context of thin shell mechanics; thickness of the mechanically relevant layer is assumed to be constant and significantly smaller than its extent in the other two dimensions. Material elements perpendicular to the surface are treated as perpendicular even after bending. We deem this approximation to be appropriate for the study of long-range effects of local tissue invagination.

To demonstrate our approach, we focus on the fruit-fly embryo. We apply SPHARM-MECH to model VFI formation in *Drosophila*. In this system, the egg shell and vitelline

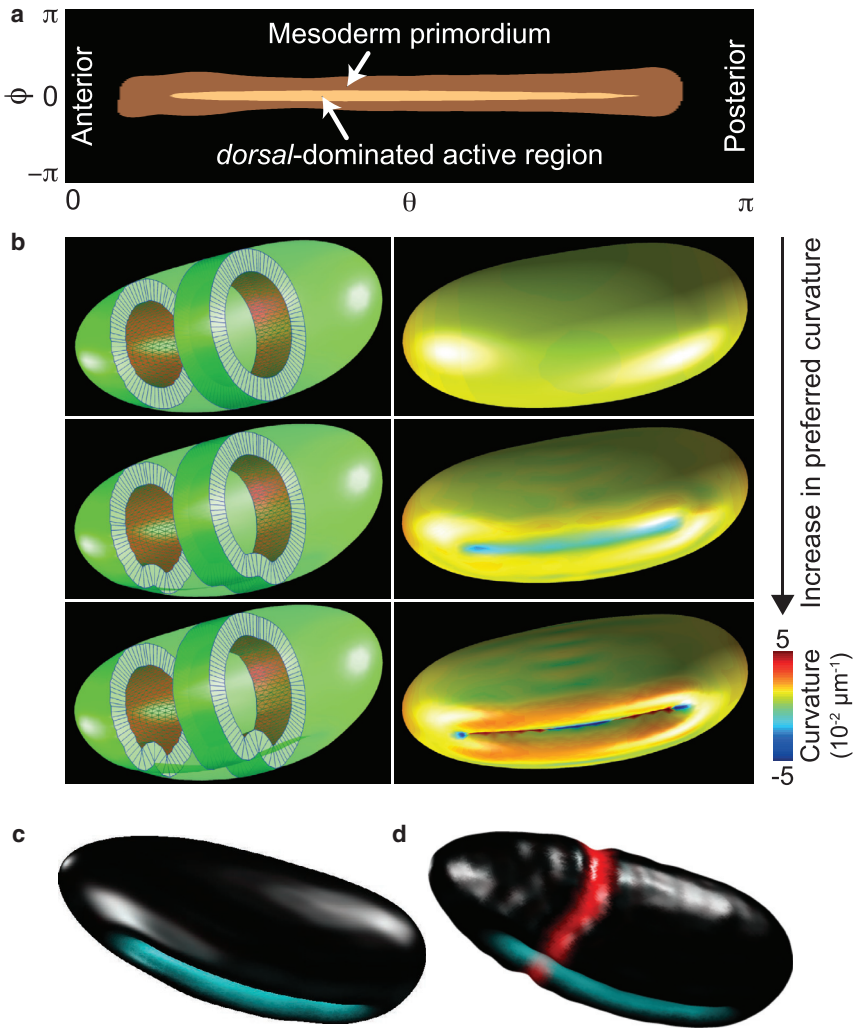

FIGURE 2 Simulation of ventral and cephalic furrows. (*a*) Given here is the mesoderm primordium region, the threshold of the map that results from the interaction of *snail*, *twist*, and *huckebein*. The threshold was chosen so the mesoderm primordium covers 16% of the total area. Area in the center shows the eight-cell-wide region defined as the activity map, based on *dorsal* and *huckebein* expression patterns, used for VFI simulations in (*b*) and (*c*) (see also the Supporting Material). Angles θ and ϕ represent the anterior-posterior and dorso-ventral positions respectively. (*b*) (*Left*) Given here are perspective views of VFI morphology predicted by SPHARM-MECH when gradually increasing the preferred curvature. (*Right*) Local mean curvature color code of corresponding morphologies is on the left. (*c*) Given here is a perspective view of the bottommost morphology of (*b*), with color showing the active region used. (*d*) Given here is a simultaneous simulation of VFI and the cephalic furrow. Colors mark the active regions.

membrane act as additional mechanical constraints. We explicitly include the vitelline membrane as a hard mechanical constraint surrounding the embryo.

We show that forces generated by the isotropic contraction of the acto-myosin meshwork local to the future mesoderm are responsible for observed tissue anisotropy on the ventral side of the embryo. We also show that these forces might encourage tissue movements of the posterior pole in the dorsal direction, thereby supporting the first phase of germ-band extension, and that this effect is directly related to the geometry of the egg.

METHODS

The software

SPHARM-MECH has been designed to enable efficient prediction of morphogenetic changes at the whole-embryo scale. This computational framework expresses the shape outline (Fig. 1 *a*) and gene expression patterns (Fig. 1 *b*) in terms of a small number of shape descriptors using the spherical harmonics basis functions (Fig. 1 *d*), calculates a configurational strain energy based on continuum shell mechanics (Fig. 1 *f*), and yields a predicted configuration that minimizes this energy (Fig. 1 *g*) by using numerical optimization. SPHARM-MECH solves the mechanical problem purely in terms of strains, requiring only one free parameter: the local preferred curvature resulting from contractile activity. This is desirable, because we rarely know details of force-generating mechanisms.

The central component of the software is a "shape_tools" library, which defines C++ classes for 1) a spherical triangular mesh, which is used for fast display, surface intersection tests, and approximate shape properties; 2) a spherical harmonics basis, which provides accurate and efficient values of basis functions as well as first and second derivatives defined on a Gaussian quadrature grid; 3) a spherical harmonics surface class, which provides accurate and efficient shape properties calculations; and 4) a shell class for continuum mechanics calculations. We also provide a development MATLAB (The MathWorks, Natick, MA) library with similar functionality.

Two applications with a graphical user interface are provided: 1) the spherical harmonics parameterization explorer, SHAPE, is a utility for inspecting, modifying, and exporting shapes; and 2) SPHARM-MECH is an interface that facilitates importing constraint and starting shapes, configuring material parameters, defining sites of mechanical activity based on gene expression, and executing energy minimization.

Details about shape properties and mechanical energy calculations are provided below (and additional details are found in the Supporting Material).

SPHARM-MECH spatial scheme

Embryo morphology and gene expression patterns are represented parametrically in functional form as

$$\vec{S} = \begin{bmatrix} x \\ y \\ z \\ \vdots \\ I_g \\ \vdots \end{bmatrix} = \begin{bmatrix} \sum_{L=0}^{\infty}\sum_{K=-L}^{L} C^x_{LK} Y_{LK}(\theta,\phi) \\ \sum_{L=0}^{\infty}\sum_{K=-L}^{L} C^y_{LK} Y_{LK}(\theta,\phi) \\ \sum_{L=0}^{\infty}\sum_{K=-L}^{L} C^z_{LK} Y_{LK}(\theta,\phi) \\ \vdots \\ \sum_{L=0}^{\infty}\sum_{K=-L}^{L} C^g_{LK} Y_{LK}(\theta,\phi) \\ \vdots \end{bmatrix}, \quad (1)$$

where θ and ϕ are spherical polar coordinates on an abstract unit sphere. $Y_{LK}(\theta,\phi)$ values are spherical harmonics functions of order L and degree K (Supporting Material). The surface outline (in the form of Cartesian coordinates) is encoded in coefficients C^x_{LK}, C^y_{LK}, and C^z_{LK}. Scalar fields I_g, encoded in coefficients C^g_{LK}, represent gene expression pattern intensities, for example, I_{snl}, I_{twi}, I_{hkb}, and I_{dfd}, as well as the activity maps that determine location and extent of changes in preferred curvature from that of an undeformed morphology. In principle, SPHARM-MECH is not limited to gene expression or activity maps, but may include other field characteristics, for example, position-dependent material properties.

The total number of coefficients for a shape outline is $3 \times (L_{\max} + 1)^2$, where $L_{\max}$ is the maximum order of the series. The infinite sum in Eq. 1 is truncated at $L_{\max} = 36$ in all simulations shown in this work. This upper limit provides sufficient accuracy, even for patterns that are highly localized, such as *ftz* and *eve* (Fig. 1 *d*; Fig. S3 *c*), and for more complex embryo morphologies (Fig. S2). Optionally, mirror symmetry can be imposed to decrease the number of shape coefficients by ~40%. Total volume, local mean curvature, shear, and stretch deformation are evaluated using numerically stable recursion relations (34). For details, see the Supporting Material.

SPHARM-MECH combines the following four characteristics: 1) a highly accurate evaluation of the spherical harmonics functions and their derivatives (34) provides reliable deformation gradient tensors and therefore shear and stretch energies, as well as accurate local mean curvatures and therefore accurate bending energies (Supporting Material); 2) fast evaluation of surface integrals is possible by Gaussian quadrature (Supporting Material); 3) a concise shape representation makes it practical to use standard techniques of numerical optimization, and the descriptors have physical meaning (see Fig. 4 *a*); and 4) the structure of the spherical harmonics representation naturally takes advantage of symmetry (Supporting Material). The main limitation of SPHARM-MECH is the restriction to shapes that are topologically equivalent to the sphere, i.e., of genus zero, and its global support (i.e., if only very local effects and local effectors are involved, then a possibly large number of harmonic functions would be needed for accurate calculations).

Finally, it should be noted that the spherical harmonics parameterization is not the only shape description appropriate for this kind of problem. Any complete set of orthogonal eigenfunctions defined on the sphere could be used. For highly localized effects, a polygonal mesh might be more appropriate. However, the four characteristics mentioned above provide the SPHARM-MECH framework with its particular computational utility for general embryogenesis problems.

Shell model and mechanical strain energy

The shell model assumed in this work is based on the Kirchhoff-Love theory of plates (35): material fibers perpendicular to the midsurface remain straight and perpendicular throughout the analysis, and shell thickness is constant. This is in contrast to Mindlin shells (36) that allow material fibers to deviate from being perpendicular to the midsurface. In this work the bending term in the strain energy density of the Kirchhoff shell, originating in the equation for the deformation gradient tensor (Supporting Material), has been replaced with the Helfrich-type bending energy. This allows us to explicitly express local deviation from preferred curvature as the primary bending constraint.

Choice of shell model defines the choice of deformation elements that will enter the analysis. To calculate deformation energy, we use a generalized neo-Hookean constitutive material model based on the work of L. R. G. Treloar for rubberlike materials (37). The strain energy density is then given by

$$\Phi = \frac{\mu}{2}\left(\overline{I_1} - 3\right) + \frac{K}{2}(J-1)^2, \quad (2)$$

where μ is the second Lame constant (shear modulus); K is the bulk modulus, $J = \lambda_1\lambda_2\lambda_3$ (determinant of the left Cauchy-Green deformation

tensor); and $\overline{I_1}$ (an invariant of the left Cauchy deformation tensor) is given by $\overline{I_1} = J^{-2/3}(\lambda_1^2 + \lambda_2^2 + \lambda_3^2)$. The principal stretches λ_i ($i = 1, 2, 3$) are calculated from shape coefficients of both current and undeformed (starting) surfaces using differential geometry (Supporting Material). The total contribution of shear and stretch energies is given by

$$E_{\text{strain}} = h\oint_{S_o} \Phi \mathrm{d}A, \tag{3}$$

where h is the thickness of the shell (assumed constant) and the integration is performed over the undeformed surface S_o. For information on evaluating Eq. 3 numerically, see the Supporting Material. The energy contribution from bending and twisting is given by

$$E_{\text{bending}} = \frac{k_b}{4}\oint_S (H - C_o)^2 \mathrm{d}A, \quad \text{with } k_b = \frac{Eh^3}{12(1-\nu^2)}, \tag{4}$$

where E is Young's modulus, ν is Poisson's ratio, H is the local mean curvature of this configuration (Supporting Material), and C_o is the preferred local mean curvature induced by gene activity. The total energy of the shell is given by

$$E_{\text{shape}} = E_{\text{strain}} + E_{\text{bending}}. \tag{5}$$

The induced preferred curvature corresponding to gene activity is not attained at the solution in the general case. It is a free parameter indirectly related to the magnitude of contractile forces: Stronger local contraction will prefer a higher curvature locally. The final morphology is always a result of a global optimization that includes constraints from the tissue as a whole.

Curvatures in all nonactive regions are constrained by experimentally obtained local curvatures, which amounts to an assumption of plasticity at long timescales. This means that for all regions for which we do not postulate a preferred curvature activity, the preferred curvature is that of the experimentally determined starting shape.

Energy minimization

Equation 5 comprises a nonlinear system. Predicted shapes are those of minimum E_{shape}, as found by using a constrained nonlinear function optimization SubPlex algorithm of the NLopt C++ library (38,39). (We have included additional (optional) nonlinear optimization approaches in the SPHARM-MECH software on an experimental basis, also with the potential that other mechanical systems might require them.)

Application example: fruit-fly ventral furrow invagination mechanics

To demonstrate the utility of SPHARM-MECH, we applied it to the problem of whole-embryo modeling of ventral furrow invagination in *Drosophila melanogaster*, a system where significant advancements in understanding gastrulation (40–42), the associated gene expression patterns, and gene product activity (13,14), have been made.

VFI formation is accompanied by a sequence of cell shape changes that ultimately lead to mesoderm internalization (41–44). The first change in shapes of cells forming the VFI is apical constriction, which is driven by acto-myosin-contraction (32,45). Apical constriction is local to expression of *twist* and *snail*, both of which are essential for furrow formation and are expressed ventrally along the anterior-posterior axis. This contraction is compatible with our assumption that preferred curvature is induced locally. *huckebein* sets the limits of *snail* and *twist* expression levels at the poles, and *dorsal* modulates relative advancement of cells in their fate (Fig. S3, *g* and *h*). We calculate two different acto-myosin contractility maps (Fig. 2 *a*), and perform a quasi-static mechanics simulation using each.

Gene expression patterns are calculated based on data from the VirtualEmbryo project (13), and from light-sheet microscopy recordings in the case of the *dorsal* expression pattern, and are assumed constant over the simulation time-frame spanning ~10 min after onset of gastrulation.

Model parameters and assumptions

Our primary model assumptions are:

1) Furrow forming forces affect the geometry through imposing a preferred curvature that is different from the preferred curvature before gene product activity starts (e.g., through contraction of cytoskeletal elements).
2) Regions of constriction cause local stiffening (larger bending resistance) relative to the passive surrounding tissue. In the chick embryo, the bending stiffness within the region of invagination-initiating cells is approximately twice as high as the surrounding tissue (27).
3) All tissue deforms passively according to a hyperelastic material model (Eq. 2).
4) The yolk is a fluid that preserves the internal volume enclosed by the embryo during deformation, and its viscosity is ignored (constant volume is enforced).
5) The vitelline membrane forms a hard constraint surrounding the embryo tissue.
6) Thin shell mechanics are sufficient to approximate the deforming surface.
7) The shell is of constant thickness h, i.e., $\lambda_3 = 1$.
8) The shell material is nearly incompressible.
9) Non-self-intersection and non-intersection with the vitelline membrane are enforced (using a triangle-triangle intersection test (46)).

The material parameters are $\nu = 0.45$ (close to that expected for water-filled tissue), $E = 100$ Pascal, $h = 0.5$ μm, $\gamma = 20$ for VFI and 10 for the cephalic furrow, and ratio of bending stiffness of the mesoderm primordium to that of the passive tissue is $\lambda = 20$ for VFI and 10 for cephalic furrow.

RESULTS AND DISCUSSION

Time-lapse, 3D image data of entire *Drosophila* embryos are recorded during gastrulation, using adaptive multiview light-sheet microscopy (47,48). Through image processing (Application-Specific Methods), this provides data of cell nuclei positions and cell shape dynamics throughout this process (Movies S1 and S2). This data is used to obtain a 3D starting morphology driving the model, as well as the time evolution of the embryo shape outline, which allows us to quantitatively assess the predictive power of the SPHARM-MECH modeling framework.

A starting surface is obtained from the outline of the blastoderm before the onset of gastrulation (Fig. 2 *b*, *top*). The local preferred curvature remains equal to that of the blastoderm everywhere except in regions of activity as determined by the activity map. Values of local preferred curvature within the activity region are input as multiples (γ) of the image-data-determined curvature ~10 min into gastrulation. In those regions, γ is increased in two steps (to 2 and 20, respectively). In each step a full numerical optimization of the strain energy is performed to yield the predicted morphology and strain field.

From previous work using electron microscopy, it is known that a core band of cells ~8–10 cell-width contracts before the rest of the mesoderm primordium region (MP) (41). Using expression patterns for *dorsal* and *huckebein* (Fig. 1, *b–d*; Fig. S3, *g* and *h*; see the Supporting Material), we find that a map corresponding to an eight-cell wide ventral anterior-posterior oriented band (Fig. 2 *a*) reproduced the initial stage of VFI qualitatively (Fig. 2, *b* and *c*) when comparing to experimental data obtained with SiMView microscopy (Movie S1) and other imaging modalities (Fig. S4). This is in contrast to the case when considering the activity of *snail*, *twist*, and *huckebein* (Supporting Material) to generate a map that is thresholded to cover 1/6 of the blastoderm surface, which is equivalent to the full MP (Fig. 2 *a*; Fig. S3 *h*, *second from bottom*). When the full MP map is used to define the region of contractility, i.e., the full MP region is contracting simultaneously, we find that the simulation does not reproduce the observed deformation even at $\gamma = 100$, but produces a frustrated ventrally slightly flattened morphology that does not invaginate. It is conceivable that constriction occurs in an outward fashion in which cells are activated as a function of stress induced by neighbors. We obtain the same result above when simulating cephalic and ventral furrow formation simultaneously (Fig. 2 *d*; and see the Supporting Material).

To observe long-range effects, we perform VFI-only simulations using SPHARM-MECH (as above with $\gamma = 20$) and estimate a predicted tissue velocity field from time points zero to ~10 min into gastrulation (Fig. 3 *a*). For comparison, experimentally observed tissue flows are extracted, by image processing, from in vivo whole-embryo data of morphogenesis recorded with SiMView microscopy, and covering the same time period (Fig. 3 *b*). Both speeds and flow directions for simulation and experiment are compared in the form of histograms. We find very good qualitative and quantitative correspondence in material velocity fields across the entire embryo, including lateral-anterior, ventro-lateral, and posterior regions that exhibit the most striking directed tissue flows (Fig. 3, *c* and *d*). Importantly, we note the dorsal flow of tissue in the posterior pole region. This flow may appear counterintuitive at first because the simulation considered deformation resulting from VFI driving forces only, and these driving forces relate to a spatial location that is distant from the affected posterior pole region. The simulation suggests that the process that forms the ventral furrow favors a dorsal movement of posterior tissue, independent of mechanisms of germ-band extension. This result is consistent with recent findings that explicitly propose that cell shape change observed during germ-band extension is a passive response to mechanical forces caused by the invaginating mesoderm (49).

To investigate the physical origin of this differential tissue flow, we take advantage of the conciseness of the spherical harmonics shape representation; in particular,

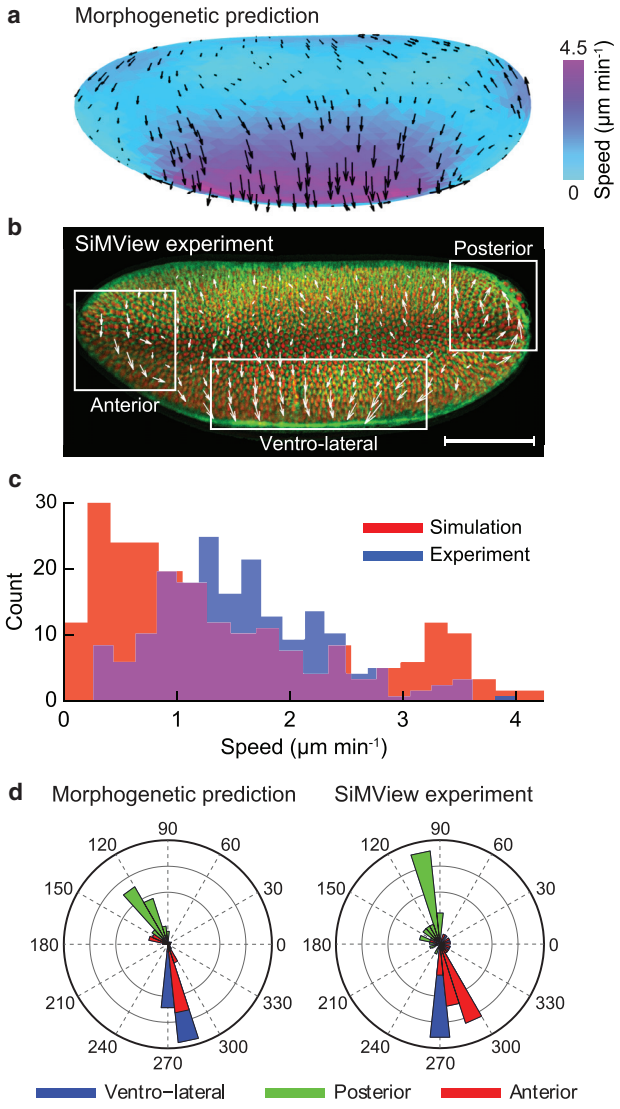

FIGURE 3 Comparison of experimentally observed and simulated tissue flows. (*a*) Given here is a tissue flow velocity field obtained from a VFI-only simulation showing speeds (color code and relative arrow size) and direction of flow. Results represent a simulation from undeformed geometry to one that equals the furrow after 10 min of onset of gastrulation. (*b*) Given here is an experimentally observed tissue flow velocity field obtained by manual tracking of 270 cell centroids, interpolated over the image over 10 min of onset of gastrulation. (*c*) Shown here is a speed histogram corresponding to simulation and experiment. (*d*) Given here are flow direction histogram angular plots corresponding to simulation (*left*) and experiment (*right*), showing resulting flow directions in the three regions outlined in (*b*). Scale bars, 100 μm.

that the fly syncytial blastoderm morphology can be reasonably approximated by only four numbers, each of which is responsible for the breaking of a different type of symmetry (Fig. 4 *a*). Using this reduced set, we perform a series of VFI simulations for symmetric and asymmetric embryo outline approximations. Six simulations are performed for each shape outline and an angular histogram for the lateral-anterior, ventro-lateral, and posterior regions

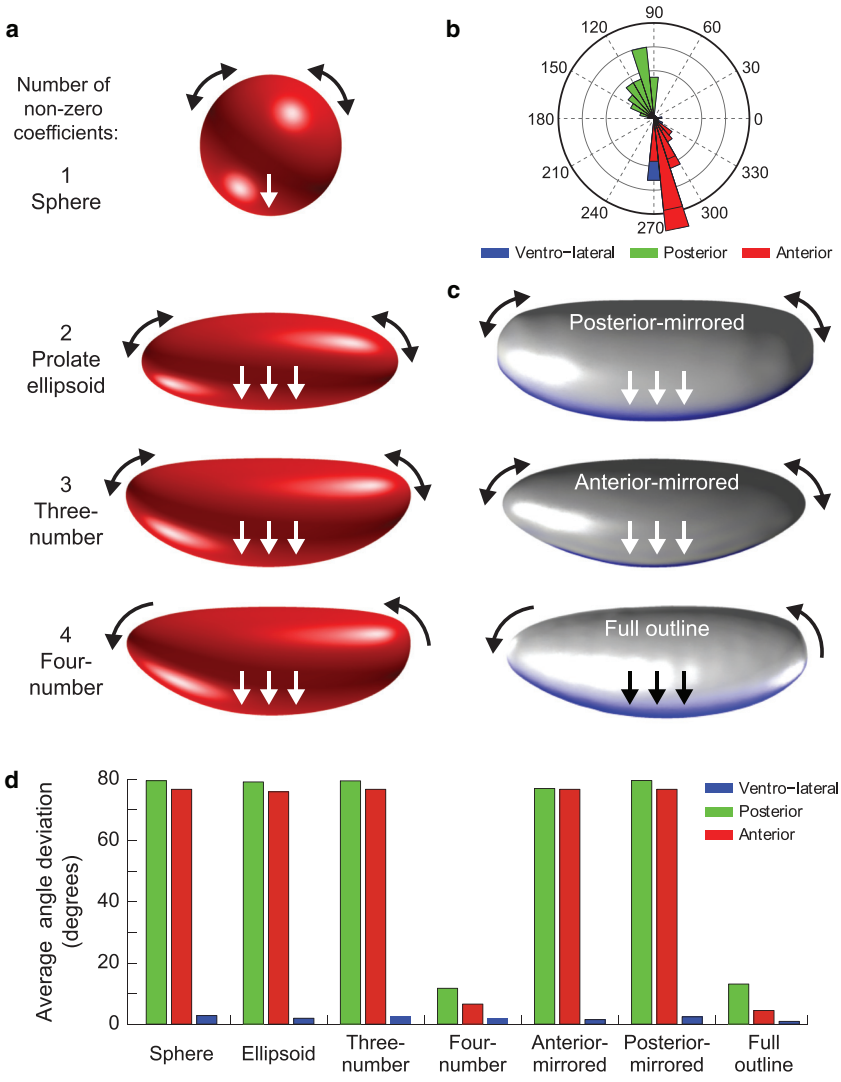

FIGURE 4 Long-range effects of embryo symmetry on tissue flows resulting from ventral furrow invagination. (*a*) Four SPHARM-MECH coefficients are sufficient to approximate the *D. melanogaster* blastoderm outline. Each coefficient breaks a different type of symmetry as seen when going from top (*sphere*) to bottom (*four-coefficient shape*). Please see the Supporting Material for more details regarding the meaning of the coefficients. When using the top three shapes (that possess *left-right*, i.e., anterior-posterior, symmetry) as base shapes for performing the VFI simulation instead of the full outline, tissue regions on the posterior (defined arbitrarily to be located on the right) flow dorsally only 50% of the time and ventrally otherwise. This is indicated by the black two-headed arrows, showing that the flow can go in either direction. In addition, the anterior and posterior flows are always with opposite destinations, i.e., when posterior tissue flows dorsally, anterior pole tissue flows ventrally and vice versa. However, when the anterior-posterior symmetry is broken (the *four-number shape*), the posterior (*lower curvature*) pole region tissue flows dorsally in all of the simulations ($n = 6$). This is indicated by the black single-headed arrows. Flow ventrally (toward the forming invagination) from the lateral sides is present in all cases. This is shown by the white arrows. (*b*) Given here is a flow direction histogram angular plot corresponding to a typical simulation with the sphere as base undeformed shape. Assuming the pole where tissue flows dorsally to be posterior, this shows flow directions similar to the ones observed in the experiment (and simulation with the full outline) (Fig. 3 *d*). Similar results are obtained for all simulations. (*c*) Two cases were constructed: a left-right symmetric outline (*top*) with the posterior features preserved (*posterior-mirrored*), and another (*middle*) with the anterior features preserved (*anterior-mirrored*). Similar to the left-right symmetry cases in (*a*), the flow was observed in each direction 50% of the time. However, when performing the VFI simulation on the full morphology repeatedly, the flow was always from the posterior dorsally, indicating that it is indeed the break in left-right symmetry that biases the direction of flow. (*d*) Given here is the plot of average ($n = 6$) flow angle deviation with respect to the experimentally observed flow. Only the simulations with shapes that possess the left-right asymmetry yield differential tissue flows close to the experimental observation.

is generated (Fig. 4 *b*). In addition to the approximate outlines, we include shapes with both their anterior and posterior features identical (*a–p* symmetric), but based on the original (experimental) outline (Fig. 4 *c*). Finally, an average deviation score, as compared to the experimental tissue flows, is calculated (Fig. 4 *d*). In all cases with *a–p* symmetric outlines, no preferred pole for the dorsal movement was observed when considering the averaged simulations. Shapes that were *a–p* asymmetric, however, showed a clear preference for dorsal movement of posterior tissue (in all cases, $n = 6$). We conclude that the break of *a–p* symmetry (nonzero value of the fourth shape parameter in Fig. 4 *a*) of the egg, coupled to the positioning and geometry of the VFI-region, are responsible for differential tissue flow.

In addition, and related to the results above, the simulated tissue flow pattern qualitatively predicts the anterior-posterior anisotropy of the tissue of the VFI, which has been observed experimentally. Using SiMView recordings of fluorescently membrane-labeled whole-embryos (Fig. 5, *a* and *b*), the data is segmented to obtain 3D cell outlines (Fig. 5 *c*). In a cross section of the embryo (cut through and orthogonal to the middle of the *a–p* axis), we observe good agreement of changes in cell shapes (experimental) versus simulated tissue deformation (Fig. 5, *c–e*). Anisotropy with respect to the *a–p* axis is calculated for all segmented cells (experimental) and from the strain field (simulated) corresponding to changes within the first 10 min of onset of gastrulation, and mapped to the embryo outline, showing good agreement (Fig. 5, *f* and *g*). It is important to note

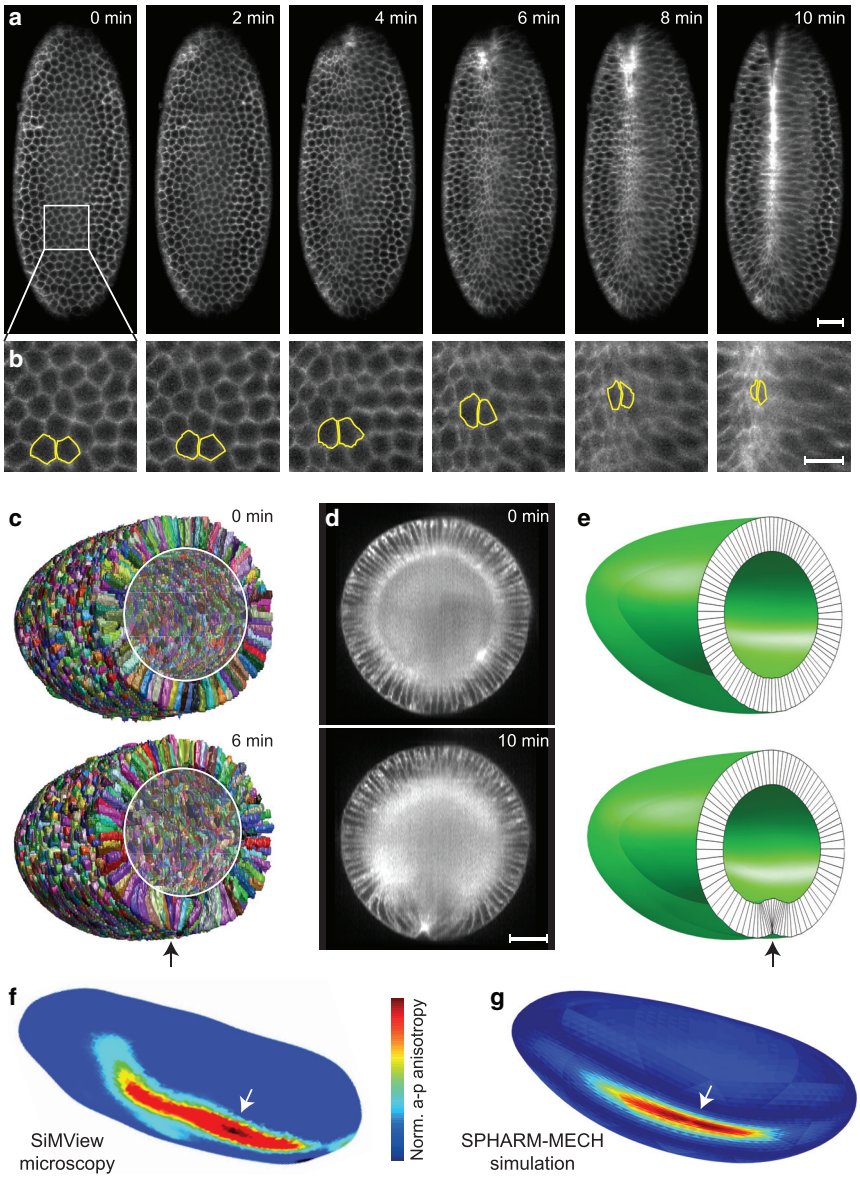

FIGURE 5 Comparison of experimentally observed and simulated tissue anisotropy. (*a*) Given here is the time sequence of Spider-GFP SiMView light-sheet microscopy images. Whole-embryo 3D stacks were recorded (Movie S1). Only one plane, which approximately cuts through the ventral furrow of each stack, is shown, with the anterior pole at the top. (*b*) Given here is an enlarged image of the region marked in (*a*) of the same time sequence, following the outlines of two neighboring cells (*yellow outlines*), and showing the development of anisotropy as the ventral furrow invagination forms. (*c*) Shown here are segmentation results for time points 0 and 6 min. (*Black arrow*) Shown here is the beginning of furrow formation. (*d*) Given here are SiMView light-sheet microscopy images of Spider-GFP (membrane label) embryos. Approximately the middle planes of the 3D stacks at time 0 and 10 min are shown. (*e*) Given here are corresponding simulation cut-through surfaces when the preferred local mean curvature of the midplane surface at the active region is increased from −0.5 (*top*) to 1.5 (*bottom*). Lines are shown as visual guides to the simulated deformation and should not be understood as cell boundaries. (*Black arrow*) Shown here is the beginning of furrow formation. (*f*) Shown here is the hole blastoderm morphology in perspective view with color code equal to *a–p* anisotropy (normalized). (White arrow) Here is the beginning of furrow formation, corresponding to the region indicated by the black arrow in (*c*). (*g*) Here, same as (*f*) performed for the simulated morphology. (*White arrow*) Here is the beginning of furrow formation, corresponding to the region indicated by the black arrow in (*e*). Scale bars, 20 μm (*a*), 10 μm (*b*), 50 μm (*d*).

that, although the outcome of the simulation is anisotropic deformation, the simulation correctly used isotropic contraction of the cytoskeleton, by enforcing an isotropic preferred curvature change. This is in accord with observed isotropic contraction of the acto-myosin meshwork determined experimentally (50). In the context of mechanical strain energy, this result can be explained as follows: due to the (isotropic) contractile forces of the actin-myosin meshwork, epithelial tissue surrounding the mesoderm primordium region is forced to extend toward the forming VFI. If this tissue is near the poles, then it has to change its curvature significantly (departing from its high preferred curvature). This comes at a high energy cost. It is easier (lower energy) for tissue to be pulled from the lateral parts of the embryo toward the furrow region, because only a relatively small change in curvature is associated with its extension toward the ventral side. This result suggests plasticity in the epithelium that sets in at a time before the onset of VFI and in which the egg serves as a scaffold, and indicates a direct mechanical influence that morphology of the egg potentially exerts on fly embryo development.

We note that at least one recent study has shown that morphogen gradients play a prominent role in fruit-fly ventral furrow invagination (51). This suggests that it might be more realistic in some cases to use morphogen gradients directly as an activation map instead of a binary activation map based on a threshold (Supporting Material).

Although all of our simulations are based on a binary activation map, which we deem sufficient for determining long-range effects, SPHARM-MECH software can easily be modified to skip the binarization filter and use a full morphogen gradient. We have included instructions

for this step in our online documentation of SPHARM-MECH. In such a case, the normalized morphogen gradient reflects the strength of the user-defined preferred curvature effect and determines its local contribution relative to the undeformed curvature (which is used by default as the local curvature for regions without morphogen activity).

Application-specific methods

Specimen preparation and live imaging

Drosophila live imaging experiments were performed with embryos homozygous for the membrane label Spider-GFP and the nuclear label His2Av-RFP. This line was constructed by combining stocks of w*; P{w[+mC] = His2Av-mRFP}; + (23560; Bloomington *Drosophila* Stock Center, Bloomington, IN) and w; +; Spider-GFP (32). Double-labeled *Drosophila* embryos were dechorionated with 50% sodium hypochlorite solution (425044; Sigma-Aldrich, St. Louis, MO) and embedded in 1% low-melting temperature agarose (SeaPlaque; Lonza, Basel, Switzerland) in a 2 mm O.D. × 20 mm glass capillary (Hilgenberg, Malsfeld, Germany) as has been previously described (47). After polymerization, the agarose cylinder was extruded just enough to expose the embryo outside of the glass capillary. The capillary holding the embryo was mounted vertically within the water-filled recording chamber of the SiMView light sheet microscope. Images were acquired at 2 min intervals. Each time point comprises two-color z-stacks recorded from four orthogonal optical views for two different physical orientations (dorso-ventral and lateral), encompassing the entire volume of the embryo with an axial step size of 1.950 μm. For all data presented, the recording was terminated when the larva hatched and crawled out of the field of view (Movie S2), after which the larva was transferred to a standard vial of fly food and raised to adulthood.

Image processing and analysis

Before multiview fusion, raw SiMView recordings were corrected for insensitive pixels on the sCMOS detectors, using median and standard deviation filters. Multiview image fusion was performed with a custom MATLAB processing pipeline, using rigid transformation for multiview stack registration followed by linear blending (47,52).

Automatic segmentation of the membrane marker channel was performed with the watershed algorithm and subsequent agglomeration of oversegmented regions by persistence-based clustering (53). To remove false positives, the nuclei marker channel was segmented with the same methodology, and a one-to-one matching between nuclei and membrane segmented regions was obtained using the Jaccard distance and the Hungarian algorithm (54). Only objects that have a unique correspondence to the nuclei channel were assumed to correspond to cells and were used in the analysis. Cell segmentations were improved manually by an expert using itkSNAP. The centroids of the segmented cells were used to construct a point-cloud. Whole-embryo morphologies were obtained by interpolation of point-cloud data (Supporting Material). Anisotropy with respect to the anterior-posterior axis was scored by approximating the cell outlines by ellipsoids, projecting the axes of these ellipsoids onto the plane parallel to the anterior-posterior axis, then projecting the result onto the anterior-posterior axis and taking the ratio of largest to smallest projection.

Summary

This work demonstrates whole-embryo mechanics modeling that is able to predict global changes in tissue flows and anisotropy based on local forces whose effect is expressed in terms of local preferred curvature. The approach was facilitated by a computational biomechanics framework that is data-driven and inherently three dimensional, accommodates a large range of morphological, gene expression and material properties, is independent of data source, and unifies its analysis within a tissue mechanics context. The software used is made available online at https://github.com/khaledkhairy/SPHARM_Mech-Project (also see the Supporting Material). Movies S3, S4, S5 and S6 provide a brief introduction to the user interface. We envision that this approach can be applied to a wide spectrum of developmental biology model systems, and will facilitate testing effects of mechanical and genetic perturbation in a biomechanical context.

SUPPORTING MATERIAL

Supporting Materials and Methods, five figures, and six movies are available at http://www.biophysj.org/biophysj/supplemental/S0006-3495(17)31244-4.

AUTHOR CONTRIBUTIONS

K.K. and P.J.K. designed research. K.K. performed research. W.L. performed imaging experiments. F.A. contributed analytic tools. K.K. analyzed data. K.K. and P.J.K. wrote the article.

ACKNOWLEDGMENTS

We thank Johannes Baumgart for his helpful comments on biomechanics modeling, Jonathan Howard for critical reading of the manuscript, Eric Wieschaus (Howard Hughes Medical Institute) for providing the Spider-GFP flies, and Aleksandra Denisin for her contributions to implementing the SiMView imaging assay.

This work was supported by the Howard Hughes Medical Institute.

REFERENCES

1. Lecuit, T., and L. Le Goff. 2007. Orchestrating size and shape during morphogenesis. *Nature*. 450:189–192.

2. Lecuit, T., and P. F. Lenne. 2007. Cell surface mechanics and the control of cell shape, tissue patterns and morphogenesis. *Nat. Rev. Mol. Cell Biol.* 8:633–644.
3. Heisenberg, C. P., and Y. Bellaïche. 2013. Forces in tissue morphogenesis and patterning. *Cell.* 153:948–962.
4. Paluch, E., and C. P. Heisenberg. 2009. Biology and physics of cell shape changes in development. *Curr. Biol.* 19:R790–R799.
5. Murrell, M., P. W. Oakes, …, M. L. Gardel. 2015. Forcing cells into shape: the mechanics of actomyosin contractility. *Nat. Rev. Mol. Cell Biol.* 16:486–498.
6. Fletcher, D. A., and R. D. Mullins. 2010. Cell mechanics and the cytoskeleton. *Nature.* 463:485–492.
7. Desprat, N., W. Supatto, …, E. Farge. 2008. Tissue deformation modulates twist expression to determine anterior midgut differentiation in Drosophila embryos. *Dev. Cell.* 15:470–477.
8. Wozniak, M. A., and C. S. Chen. 2009. Mechanotransduction in development: a growing role for contractility. *Nat. Rev. Mol. Cell Biol.* 10:34–43.
9. Howard, J., S. W. Grill, and J. S. Bois. 2011. Turing's next steps: the mechanochemical basis of morphogenesis. *Nat. Rev. Mol. Cell Biol.* 12:392–398.
10. Keller, P. J. 2013. Imaging morphogenesis: technological advances and biological insights. *Science.* 340:1234168.
11. Khairy, K., and P. J. Keller. 2011. Reconstructing embryonic development. *Genesis.* 49:488–513.
12. Pantazis, P., and W. Supatto. 2014. Advances in whole-embryo imaging: a quantitative transition is underway. *Nat. Rev. Mol. Cell Biol.* 15:327–339.
13. Fowlkes, C. C., C. L. Hendriks, …, J. Malik. 2008. A quantitative spatiotemporal atlas of gene expression in the Drosophila blastoderm. *Cell.* 133:364–374.
14. Tomancak, P., B. P. Berman, …, G. M. Rubin. 2007. Global analysis of patterns of gene expression during Drosophila embryogenesis. *Genome Biol.* 8:R145.
15. Wyczalkowski, M. A., Z. Chen, …, L. A. Taber. 2012. Computational models for mechanics of morphogenesis. *Birth Defects Res. C Embryo Today.* 96:132–152.
16. Misra, M., B. Audoly, …, S. Y. Shvartsman. 2016. Shape transformations of epithelial shells. *Biophys. J.* 110:1670–1678.
17. Brodland, G. W., V. Conte, …, M. Miodownik. 2010. Video force microscopy reveals the mechanics of ventral furrow invagination in Drosophila. *Proc. Natl. Acad. Sci. USA.* 107:22111–22116.
18. Conte, V., F. Ulrich, …, M. Miodownik. 2012. A biomechanical analysis of ventral furrow formation in the Drosophila melanogaster embryo. *PLoS One.* 7:e34473.
19. Odell, G. M., G. Oster, …, B. Burnside. 1981. The mechanical basis of morphogenesis. I. Epithelial folding and invagination. *Dev. Biol.* 85:446–462.
20. Lye, C. M., G. B. Blanchard, …, B. Sanson. 2015. Mechanical coupling between endoderm invagination and axis extension in Drosophila. *PLoS Biol.* 13:e1002292.
21. Rauzi, M., U. Krzic, …, M. Leptin. 2015. Embryo-scale tissue mechanics during Drosophila gastrulation movements. *Nat. Commun.* 6:8677.
22. He, B., K. Doubrovinski, …, E. Wieschaus. 2014. Apical constriction drives tissue-scale hydrodynamic flow to mediate cell elongation. *Nature.* 508:392–396.
23. Conte, V., J. J. Muñoz, and M. Miodownik. 2008. A 3D finite element model of ventral furrow invagination in the *Drosophila melanogaster* embryo. *J. Mech. Behav. Biomed. Mater.* 1:188–198.
24. Allena, R., A. S. Mouronval, and D. Aubry. 2010. Simulation of multiple morphogenetic movements in the Drosophila embryo by a single 3D finite element model. *J. Mech. Behav. Biomed. Mater.* 3:313–323.
25. Taber, L. A. 2009. Towards a unified theory for morphomechanics. *Philos. Transact. A Math Phys. Eng. Sci.* 367:3555–3583.
26. Davidson, L. A., M. A. Koehl, …, G. F. Oster. 1995. How do sea urchins invaginate? Using biomechanics to distinguish between mechanisms of primary invagination. *Development.* 121:2005–2018.
27. Varner, V. D., D. A. Voronov, and L. A. Taber. 2010. Mechanics of head fold formation: investigating tissue-level forces during early development. *Development.* 137:3801–3811.
28. Vasiev, B., A. Balter, …, C. J. Weijer. 2010. Modeling gastrulation in the chick embryo: formation of the primitive streak. *PLoS One.* 5:e10571.
29. Styner, M., J. A. Lieberman, …, G. Gerig. 2005. Morphometric analysis of lateral ventricles in schizophrenia and healthy controls regarding genetic and disease-specific factors. *Proc. Natl. Acad. Sci. USA.* 102:4872–4877.
30. Paniagua, B., L. Cevidanes, …, M. Styner. 2011. Outcome quantification using SPHARM-PDM toolbox in orthognathic surgery. *Int. J. CARS.* 6:617–626.
31. Shen, L., H. Farid, and M. A. McPeek. 2009. Modeling three-dimensional morphological structures using spherical harmonics. *Evolution.* 63:1003–1016.
32. Martin, A. C., M. Kaschube, and E. F. Wieschaus. 2009. Pulsed contractions of an actin-myosin network drive apical constriction. *Nature.* 457:495–499.
33. Wang, Y. C., Z. Khan, …, E. F. Wieschaus. 2012. Differential positioning of adherens junctions is associated with initiation of epithelial folding. *Nature.* 484:390–393.
34. Bosh, W. 2000. On the computation of derivatives of Legendre functions. *Phys. Chem. Earth.* 25:655–659.
35. Love, E. H. 1888. The small free vibrations and deformations of elastic shells. *Phil. Trans. R. Soc. A.* 17:491–546.
36. Mindlin, R. D. 1951. Influence of rotatory inertia and shear on flexural motions of isotropic, elastic plates. *J. Appl. Mechanics.* 18:31–38.
37. Treloar, L. R. G. 1948. Stresses and birefringence in rubber subjected to general homogenous strain. *Proc. Phys. Soc.* 60:135–144.
38. Johnson, S. G. The NLopt nonlinear-optimization package. https://nlopt.readthedocs.io/en/latest/
39. Rowan, T. 1990. Functional Stability Analysis of Numerical Algorithms. PhD thesis. University of Texas, Austin, TX.
40. Leptin, M. 1995. Drosophila gastrulation: from pattern formation to morphogenesis. *Annu. Rev. Cell Dev. Biol.* 11:189–212.
41. Leptin, M., and B. Grunewald. 1990. Cell shape changes during gastrulation in Drosophila. *Development.* 110:73–84.
42. Sweeton, D., S. Parks, …, E. Wieschaus. 1991. Gastrulation in Drosophila: the formation of the ventral furrow and posterior midgut invaginations. *Development.* 112:775–789.
43. Costa, M., E. T. Wilson, and E. Wieschaus. 1994. A putative cell signal encoded by the folded gastrulation gene coordinates cell shape changes during Drosophila gastrulation. *Cell.* 76:1075–1089.
44. Keller, R., L. A. Davidson, and D. R. Shook. 2003. How we are shaped: the biomechanics of gastrulation. *Differentiation.* 71:171–205.
45. Leptin, M. 1991. twist and snail as positive and negative regulators during Drosophila mesoderm development. *Genes Dev.* 5:1568–1576.
46. Möller, T. 1997. A fast triangle-triangle intersection test. *J. Graphics Tools.* 2:25–30.
47. Tomer, R., K. Khairy, …, P. J. Keller. 2012. Quantitative high-speed imaging of entire developing embryos with simultaneous multiview light-sheet microscopy. *Nat. Methods.* 9:755–763.
48. Royer, L. A., W. C. Lemon, …, P. J. Keller. 2016. Adaptive light-sheet microscopy for long-term, high-resolution imaging in living organisms. *Nat. Biotechnol.* 34:1267–1278.

49. Butler, L. C., G. B. Blanchard, …, B. Sanson. 2009. Cell shape changes indicate a role for extrinsic tensile forces in Drosophila germ-band extension. *Nat. Cell Biol.* 11:859–864.

50. Martin, A. C., M. Gelbart, …, E. F. Wieschaus. 2010. Integration of contractile forces during tissue invagination. *J. Cell Biol.* 188:735–749.

51. Heer, N. C., P. W. Miller, …, A. C. Martin. 2017. Actomyosin-based tissue folding requires a multicellular myosin gradient. *Development.* 144:1876–1886.

52. Amat, F., B. Höckendorf, …, P. J. Keller. 2015. Efficient processing and analysis of large-scale light-sheet microscopy data. *Nat. Protoc.* 10:1679–1696.

53. Chazal, F., L. J. Guibas, …, P. Skraba. 2009. Persistence-Based Clustering in Riemannian Manifolds, Research Report 6968. French Institute for Research in Computer Science and Automation, Rocquencourt, France.

54. Kuhn, H. W. 1955. The Hungarian method for the assignment problem. *Nav. Res. Logist.* 2:83–97.

Biophysical Journal, Volume *114*

Supplemental Information

A Preferred Curvature-Based Continuum Mechanics Framework for Modeling Embryogenesis

Khaled Khairy, William Lemon, Fernando Amat, and Philipp J. Keller

Supplementary Notes

Supplementary Note 1	The spherical harmonics
Supplementary Note 2	Calculation of associated Legendre functions and their derivatives
Supplementary Note 3	Calculation of surface properties
Supplementary Note 4	Numerical integration using Gaussian quadrature
Supplementary Note 5	From point cloud to spherical harmonics parameterization
Supplementary Note 6	Calculation of the shear and stretch strain energy
Supplementary Note 7	Meaning of the spherical harmonics coefficients and shape symmetry in the context of the fruit fly blastoderm outline
Supplementary Note 8	Definition of the mesoderm primordium and local contractile activity region for VFI
Supplementary Note 9	Computer programs
Supplementary Note 10	Dimensions of the fruit fly embryo
Supplementary Note 11	Simultaneous simulation of multiple events

Supplementary Videos

Supplementary Video 1	SiMView time-lapse recording of fruit fly embryo undergoing gastrulation
Supplementary Video 2	Control for physiological development after multi-color multi-angle SiMView time-lapse imaging
Supplementary Video 3	Brief introduction to SHAPE
Supplementary Video 4	Brief introduction to SPHARM-MECH (part 1)
Supplementary Video 5	Brief introduction to SPHARM-MECH (part 2)
Supplementary Video 6	Brief introduction to SPHARM-MECH (part 3)

Supplementary Note 1 | The spherical harmonics

The spherical harmonics expansion of a function $r(\theta,\phi)$ in spherical polar coordinates(θ,ϕ) is,

$$r(\theta,\phi)=\sum_{L}^{\infty}\sum_{K=-L}^{L}C_{LK}Y_{LK}(\theta,\phi)$$

where

$$Y_{LK}(\theta,\phi)=N_{LK}\cdot P_{LK}(\cos\theta)e^{iK\phi}$$

with $P_{LK}(\cos\theta)$ the associated Legendre functions and N_{LK} normalization constants. *L* and *K* are integers, $0\le\theta\le\pi$ and$-\pi\le\phi\le\pi$. It is more straightforward to work with real functions, therefore we define the real symmetric and anti-symmetric combinations of the above functions (Supplementary Figure 1), $y(\theta,\phi)$,

$$y_{LK}(\theta,\phi)=\bar{P}_{LK}(\cos\theta)\cos(K\phi)$$

for $K\ge 0$, and

$$y_{LK}(\theta,\phi)=\bar{P}_{LK}(\cos\theta)\sin(|K|\phi)$$

for $K<0$, where $\bar{P}_{LK}(x)$ is given by

$$\bar{P}_{LK}(x)=\sqrt{(2-\delta_{0K})\cdot(2L+1)\cdot\frac{(L-K)!}{(L+K)!}}\cdot P_{LK}(x)$$

where we used the normalization given in Heiskanen and Moritz[1]. Also,

$$P_{LK}(x)=(1-x^2)^{K/2}\frac{d^K}{dx^K}\cdot P_L(x)$$

where

$$P_L(x)=\frac{1}{2^L\cdot L!}\cdot\frac{d^L}{dx^L}(x^2-1)^L$$

Note that the factor $(-1)^K$, called the "Condon-Shortly phase factor", is not included in our definition. Also $P_{L0}(x)=P_L(x)$.

The expressions for $P_{LK}(\cos\theta)$ for up to *L=2* are given below ($x=\cos(\theta)$):

$P_{00}(x)=1$	$P_{10}(x)=x$ $P_{11}(x)=\sin\theta$	$P_{20}(x)=\frac{1}{2}(3x^2-1)$ $P_{21}(x)=3\cos\theta\sin\theta$ $P_{22}(x)=3\sin^2\theta$

Supplementary Note 2 | Calculation of associated Legendre functions and their derivatives

For constructing the basis it is necessary to calculate the associated Legendre functions efficiently and accurately. For the calculation of geometric properties, it is also necessary to calculate the derivatives up to order two. This is done by using efficient and numerically stable recursion expressions[2, 3].

The $P_{L,K}$ are calculated using backward recursion relations[3]. For each integer $L \geq 0$ the value of $P_{L,K}(\cos\theta)$ is evaluated using the relations

$$P_{L,L}(\cos(\theta)) = \frac{(2L)!}{L!}\left(\frac{1}{2}\sin\theta\right)^L$$

and

$$P_{L,K+2}(\cos\theta) = (2K+1)\cdot\cot(\theta)P_{L,K+1}(\cos\theta) - (L-K)(L+K+1)P_{L,K}(\cos\theta)$$

where $P_{L,K}(\cos\theta) = 0$ when $K > L$.

The derivatives of order k for the associated Legendre polynomials with respect to θ are obtained by the following relations[2, 4] (provided here without the normalization):

$$2\frac{d^k}{d\theta^k}P_{LK}(\cos\theta) = (L+K)\cdot(L-K+1)\cdot\frac{d^{k-1}}{d\theta^{k-1}}P_{L,K-1}(\cos\theta) - \frac{d^{k-1}}{d\theta^{k-1}}P_{L,K+1}(\cos\theta)$$

where

$$\frac{d^k}{d\theta^k}P_{L0}(\cos\theta) = -\frac{d^{k-1}}{d\theta^{k-1}}P_{L,1}(\cos\theta) \text{ and } \frac{d^k}{d\theta^k}P_{LL}(\cos\theta) = L\frac{d^{k-1}}{d\theta^{k-1}}P_{L,L-1}(\cos\theta)$$

These relations are stable for low order derivatives and efficient for computation, because the derivative expressions do not introduce additional trigonometric function evaluations.

Supplementary Note 3 | Calculation of surface properties

The surface outline (without gene expression patterns) is represented parametrically as

$$\vec{\boldsymbol{S}} = \begin{bmatrix} \boldsymbol{x}(\boldsymbol{\theta},\boldsymbol{\phi}) \\ \boldsymbol{y}(\boldsymbol{\theta},\boldsymbol{\phi}) \\ \boldsymbol{z}(\boldsymbol{\theta},\boldsymbol{\phi}) \end{bmatrix} = \begin{bmatrix} \sum_{\boldsymbol{L}=\boldsymbol{0}}^{\infty} \sum_{\boldsymbol{K}=-\boldsymbol{L}}^{\boldsymbol{L}} \boldsymbol{C}_{\boldsymbol{LK}}^{\boldsymbol{X}} \boldsymbol{Y}_{\boldsymbol{LK}}(\boldsymbol{\theta},\boldsymbol{\phi}) \\ \sum_{\boldsymbol{L}=\boldsymbol{0}}^{\infty} \sum_{\boldsymbol{K}=-\boldsymbol{L}}^{\boldsymbol{L}} \boldsymbol{C}_{\boldsymbol{LK}}^{\boldsymbol{Y}} \boldsymbol{Y}_{\boldsymbol{LK}}(\boldsymbol{\theta},\boldsymbol{\phi}) \\ \sum_{\boldsymbol{L}=\boldsymbol{0}}^{\infty} \sum_{\boldsymbol{K}=-\boldsymbol{L}}^{\boldsymbol{L}} \boldsymbol{C}_{\boldsymbol{LK}}^{\boldsymbol{Z}} \boldsymbol{Y}_{\boldsymbol{LK}}(\boldsymbol{\theta},\boldsymbol{\phi}) \end{bmatrix}$$

Surface properties are computed from partial derivatives of the surface functions using equations of classical differential geometry[5]. We provide this background here for completeness, and as applied to our spherical harmonics surface parameterization.

The surface normal is given by

$$\hat{n} = \frac{\vec{S}_\theta \times \vec{S}_\phi}{|\vec{S}_\theta \times \vec{S}_\phi|}$$

where $\vec{S}_\theta$ and $\vec{S}_\phi$ are now the 3-vectors,

$$\vec{S}_\theta = \begin{bmatrix} \sum_{L=0}^{\infty} \sum_{K=-L}^{L} C_{LK}^{X} \frac{\partial Y_{LK}(\theta,\phi)}{\partial \theta} \\ \sum_{L=0}^{\infty} \sum_{K=-L}^{L} C_{LK}^{Y} \frac{\partial Y_{LK}(\theta,\phi)}{\partial \theta} \\ \sum_{L=0}^{\infty} \sum_{K=-L}^{L} C_{LK}^{Z} \frac{\partial Y_{LK}(\theta,\phi)}{\partial \theta} \end{bmatrix}$$

similarly for $\vec{S}_\phi$, and the second derivatives (calculated using the recursion relations given above).

The total surface area A is given by

$$A = \int dA = \int_0^{\pi} \int_0^{2\pi} |\vec{S}_\theta \times \vec{S}_\phi| d\theta d\phi$$

The total volume V is given by

$$V = \frac{1}{3} \int_0^{\pi} \int_0^{2\pi} (\vec{S} \cdot \hat{n}) |\vec{S}_\theta \times \vec{S}_\phi| d\theta d\phi$$

In general, many quantities related to surfaces are calculated from the coefficients of the first and second fundamental forms. The first fundamental form is given by

$$I = d\vec{S} \cdot d\vec{S}$$
$$I = E d\theta^2 + 2F d\theta d\phi + G d\phi^2$$

The second fundamental form is

$$II = -d\vec{S} \cdot d\hat{n}$$
$$II = Ld\theta^2 + 2Md\theta d\phi + Nd\phi^2$$

The coefficients of the first (*E*, *F*, *G*) and second (*L*, *M*, *N*) fundamental forms are given in terms of the surface differentials and normals by

$$E = \vec{S}_\theta \cdot \vec{S}_\theta$$
$$F = \vec{S}_\theta \cdot \vec{S}_\phi$$
$$G = \vec{S}_\phi \cdot \vec{S}_\phi$$
$$L = \vec{S}_{\theta\theta} \cdot \hat{n}$$
$$M = \vec{S}_{\theta\phi} \cdot \hat{n}$$
$$N = \vec{S}_{\phi\phi} \cdot \hat{n}$$

We calculate the local mean curvature *H* as

$$H = \frac{EN + GL - 2FM}{2(EG - F^2)}$$

which is needed for calculating the bending energy (Eq. 4 in **Online Methods**).
An important self-check for the accuracy of our shape property calculations is the Gaussian curvature (*K*),

$$K = \frac{LN - M^2}{EG - F^2}$$

which when integrated over a closed surface of spherical topology must satisfy

$$k = \frac{1}{4\pi} \int_{\vec{S}} K dA = 1$$

Supplementary Note 4 | Numerical integration using Gaussian quadrature

The integrals needed for area, volume and total Gaussian curvature cannot be evaluated analytically. A, V and k are calculated using numerical integration by Gaussian quadrature[6]. If a function f is to be integrated from -1 to 1, and a Gaussian quadrature of order N is chosen, then

$$\int_{-1}^{1} f(x)dx \approx \sum_{n=1}^{N} f_n w_n$$

where the function is evaluated at the points x_n, $-1 < x_n < 1$, and w_n are the Gaussian quadrature weights. If the integration limits are instead a and b, then one uses the linear transformation

$$x_n' = \frac{1}{2}(b-a)x_n + \frac{1}{2}(b+a)$$

f is evaluated at these new points.

We developed computer code that generates the Gaussian quadrature base-points and uses them to calculate all shape properties, deformation gradient tensor, and the coefficients of the first and second fundamental forms (**Supplementary Note 9**).

Supplementary Note 5 | From point cloud to spherical harmonics parameterization

We interpolate the point-cloud, that represents a surface, by using radial basis functions[7], which provide a description that contains roughly as many coefficients as there are points in the point-cloud (~6,000). Next we calculate a high quality isosurfacing of the radial basis functions[8], which yields a triangular mesh with approximately equilateral triangles. This mesh is subsequently mapped to the unit sphere using techniques described elsewhere[9]. From that mapping, we calculate the spherical harmonics (Fourier) coefficients that correspond to individual Cartesian coordinates x, y and z, using linear least squares fitting[10]. In similar fashion any scalar field (for example gene expression pattern) originally associated with the point cloud is evaluated by using the identical mapping above.

Gene expression patterns can also be mapped onto the unit sphere from two-dimensional images of expression patterns (interpreted as an angular chart). These patterns are then transformed (rotated) canonically and interpreted as maps on an arbitrary morphology. This technique requires careful registration of the pattern to the underlying morphology, but has the power of making encoding and manipulation of expression patterns be independent of the recording of the shape outlines.

Supplementary Note 6 | Calculation of the shear and stretch strain energy

The shear and stretch strain energy is calculated as (see Eq. 2 and 3 in **Methods**):

$$E_{\text{strain}} = h \oint_{S_o} \frac{\mu}{2}(\overline{I_1} - 3) + \frac{K}{2}(J-1)^2 dA$$

where K is the bulk modulus, μ the shear modulus, and the quantities $J = \lambda_1\lambda_2\lambda_3$ and $\overline{I_1} = J^{-2/3}(\lambda_1^2 + \lambda_2^2 + \lambda_3^2)$ are calculated from the principal stretches λ_i (i = 1, 2, 3). As we are assuming constant shell thickness, we set $\lambda_3 = 1$. The principal stretches are obtained from the square root of the eigenvalues λ_i (i = 1, 2, 3) of $F^T \cdot F$, where F represents the shear and stretch component of the deformation gradient tensor and is approximated as:

$$F = \vec{S}_\theta \otimes \vec{\bar{S}}^\theta + \vec{S}_\phi \otimes \vec{\bar{S}}^\phi$$

Here, $\otimes$ is the Kronecker product, $\vec{S}_\theta$ is the tangent with respect to the θ coordinate for the deformed surface, the subscript θ indicates that the vector is member of the natural (covariant) basis. $\vec{\bar{S}}^\theta$ is the tangent with respect to the θ coordinate for the undeformed surface, the superscript θ indicates that the vector is member of the reciprocal (contravariant) basis. The same notation applies to the ϕ coordinate in the second term. These quantities are calculated using the formulas of **Supplementary Notes 2** and **3**. Direct relations to coefficients of the fundamental forms also exist. For more information, the reader is referred to texts in solid mechanics[11] and shell mechanics[12].

Supplementary Note 7 | Meaning of the spherical harmonics coefficients and shape symmetry in the context of the fruit fly blastoderm outline

The spherical harmonics coefficients for small L values can be directly interpreted in terms of morphological features of the embryo. Since in the following we will mention specific coefficients, we first find for every shape used in this work the transformation (rotation and translation) that renders it in canonical form. This transformation is determined using the method of Brechbueler *et al*.[13]. It is based on the values of the $L = 1$ coefficients (and can be achieved by using the command "s = r_inv(s)" in the supplied Matlab library). In the following we will assume that the shape has been transformed to this canonical form. The $L = 0$ coefficients, i.e. C^x_{00}, C^y_{00} and C^z_{00}, indicate the x y z coordinates of the center of mass of the shape (embryo) in Cartesian space. These are usually set to zero. The three coefficients $C^x_{0\text{-}1}$, C^y_{10} and C^z_{11} determine the dimensions of the ellipsoid that approximates the embryo morphology with $C^x_{0\text{-}1} < 0$ and $|C^x_{0\text{-}1}| > C^y_{10} > C^z_{11} > 0$ (**Supplementary Fig. 5a**). C^z_{20} determines the extent of the dorso-ventral asymmetry and simultaneously the relative flattening of the dorsal side. The extent of tapering at the poles is determined by C^y_{30} and C^y_{50}, and the anterior-posterior asymmetry by C^y_{20} and C^y_{40}. The reader is encouraged to execute the supplied program SHAPE to experiment with these coefficients and to develop a feeling for their meanings.

The spherical harmonics can elegantly incorporate symmetry by pruning the basis set in a preset fashion. For the above canonical configuration, to achieve mirror symmetry across the y-z plane that passes through the center of mass, only C^x_{LK} values with $K < 0$ and C^y_{LK} and C^z_{LK} values with $K \geq 0$ need to be considered. The reader is encouraged to test this using SHAPE. For shapes that require L values > 24 enforcing mirror symmetry reduces the parameter space by about 40%. Such a reduction is important (and strongly recommended) during the optimization. Therefore SPHARM-MECH provides the user with an option to enforce the mirror-symmetry.

Supplementary Note 8 | Definition of the mesoderm primordium and local contractile activity region for VFI

The mesoderm primordium region (MP) is composed of ~1,000 cells located ventrally along the anterior-posterior axis[14, 15]. Assuming approximately equal apical cell areas for the late blastoderm stage, the MP thus occupies ~16% of the total surface area. Its exact location and boundaries are taken as regions of overlapping expressions of *twist* and *snail*. *huckebein* sets the anterior and posterior borders of MP by suppression of *snail* posteriorly, and antagonizing activation of *twist* and *snail* target genes anteriorly. In the present work, the exact boundary for the MP region is determined, using the normalized local *twist*, *snail* and *huckebein* expression levels $\overline{I_{\text{snail}}}$, $\overline{I_{\text{twist}}}$ and $\overline{I_{\text{huckebein}}}$ respectively (**Fig. 2a** and **Supplementary Fig. 3h**), by setting locations with

$$\overline{I_{\text{snail}}}^{\alpha} \times \overline{I_{\text{twist}}}^{\beta} \times \overline{f(I_{\text{huckebein}}, \gamma)} > \epsilon$$

equal to one, and zero elsewhere. α, β and γ are hyperparameters that we set to 1.0. The threshold value ϵ is set such that MP occupies 16% of the total surface area. $\overline{f(I_{\text{huckebein}}, \gamma)}$ is an exponential decay function with $\overline{f(I_{\text{huckebein}}, \gamma)} = e^{-\gamma \overline{I_{\text{huckebein}}}}$.

Gene expression patterns for *twist*, *snail* and *huckebein* are obtained from the VirtualEmbryo project database[16] for the latest available stage before gastrulation.

The activity map for initiation of VFI formation that is used in all simulations is provided by $\overline{I_{\text{dorsal}}}^{\alpha} \times f(I_{\text{huckebein}}, \gamma) > \epsilon$, where the value ϵ is set such that the activity map covers an area corresponding to an 8-cell wide band (**Fig. 2a**).

Supplementary Note 9 | Computer programs

SPHARM-MECH calculations can be performed on a conventional computer workstation. The compiled software for viewing and manipulating SPHARM surfaces (**Supplementary Fig. 5a**) and for performing SPHARM-MECH calculations (**Supplementary Fig. 5b**) are provided as github repositories at:

- Shape tools: C/C++ classes and utility functions for calculating spherical harmonics basis functions and their derivatives, and for generating and representing SPHARM objects and the SPHARM-MECH shell object. Github repository: https://github.com/khaledkhairy/shape_tools
- SHAPE (**S**pherical **HA**rmonics **P**arameterization **E**xplorer): Application with VTK/QT GUI for manipulating and viewing surfaces and testing the accuracy of C/C++ classes. Github repository: https://github.com/khaledkhairy/SHAPE
- SPHARM-MECH (generalization of the SPHARM approach for mechanics): Application with VTK/QT GUI for performing mechanics simulations. Github repository: https://github.com/khaledkhairy/SPHARM_Mech-Project

Please see **Supplementary Videos 3-6** for an introduction to the user interface.

Supplementary Note 10 | Dimensions of the fruit fly embryo

1. Average dimensions
   a. Length of longest axis[17]: 0.51 ± 0.003 mm (n = 43).
   b. Length of longest axis for standard averaged embryo from the Virtual Embryo Project[16]: 0.40 mm. *Note*: Measurements are based on images of *in situ* hybridized embryos and are therefore expected to be lower than for live images.
   c. Length of short axis[17]: 0.18 ± 0.001 mm (n = 43).
2. Volume
   a. Assuming an ellipsoid of volume given by 1/6 x π x Width^2 x Length (Markow *et al.*[17]): 9.02 ± 0.14 x 10^{-3} mm^3 (n = 43). Values are expected to be higher than true volume due to the ellipsoid approximation.
   b. In case of the Virtual Embryo Project[16] dataset, the volume enclosed by the vitteline membrane is estimated to be 5.56 x 10^{-3} mm^3 when assuming an average distance of 5 μm between cell centers and apical side. (Using the exact outline that coincides with the cell centers, we obtain 4.38 x 10^{-3} mm^3).
   c. Our own reconstructed embryos using live imaging techniques described in Tomer *et al.*[18] and Royer *et al.*[19] yield a vitteline membrane enclosed volume of 6.70 x 10^{-3} mm^3 (n = 2).
3. Surface area of outline
   a. Markow *et al.*[17]: 0.237 mm^2. The surface area is again based on the ellipsoid approximation. It is expected to exceed the true value for simple geometries, i.e. before gastrulation.
   b. Using exact outline that coincides with the cell centers, from the Virtual Embryo Project[16] dataset we obtain 0.1492 mm^2.
   c. Our own reconstructed embryos using live imaging techniques described in Tomer *et al.*[18] and Royer *et al.*[19] yield 0.21 mm^2 (n = 2).

Supplementary Note 11 | Simultaneous simulation of multiple events

The SHARM-MECH modeling approach is applicable to simultaneous simulation of multiple folds. We simulate, in addition to the formation of VFI, simultaneously the cephalic furrow (CF) (**Fig. 1g,h**). The mechanism underlying CF formation is currently unknown, however, *deformed* (*dfd*) is expressed in cells of the CF and its expression pattern can be used to approximate the region of folding activity (**Fig. 1b-d** and **Supplementary Fig. 3d-f,h**). We assume – just as with the VFI – that the CF forms as a consequence of departure of the local preferred curvature from that of the blastoderm. SPHARM-MECH is then able to perform a data-driven simulation for both VFI and CF formation simultaneously (**Fig. 2d**).

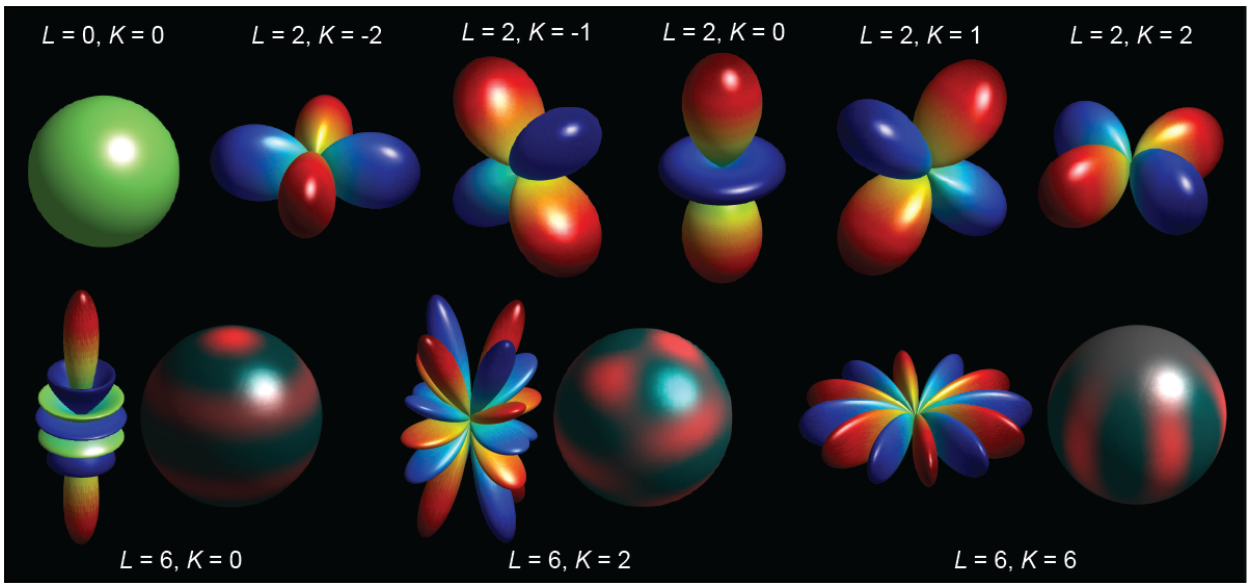
L = 0, K = 0
L = 2, K = -2
L = 2, K = -1
L = 2, K = 0
L = 2, K = 1
L = 2, K = 2
L = 6, K = 0
L = 6, K = 2
L = 6, K = 6

Supplementary Figure 1 | Spherical harmonics basis functions

Examples of spherical harmonics basis functions (**Supplementary Note 1**). These functions are well known as the angular portion of a set of solutions to Laplace's equation. Color code: blue negative to red positive values. In the bottom row a perspective view of is shown left of the corresponding mapping of function values to the unit sphere.

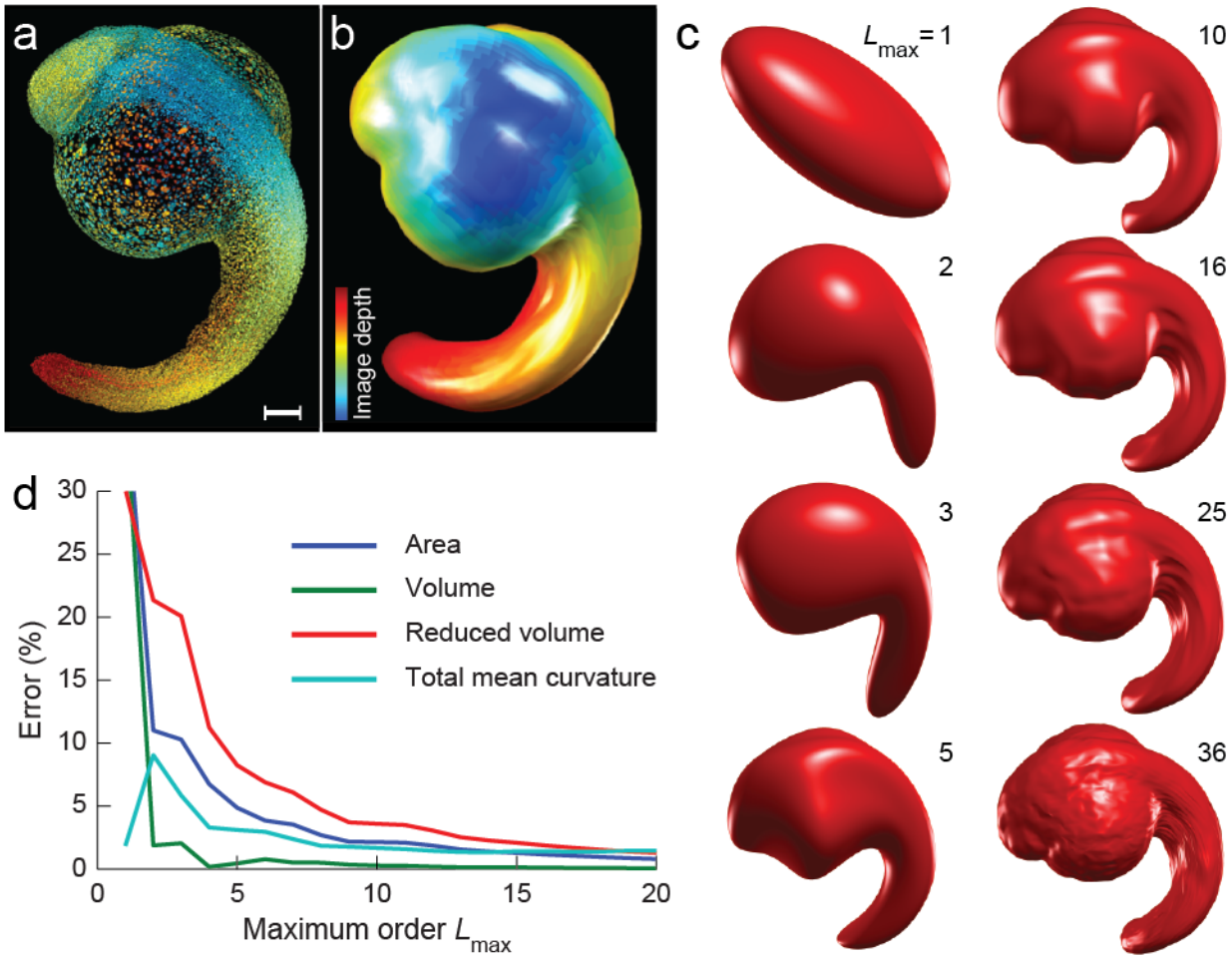
a
b
Image depth
c
L_{max} = 1
10
2
16
3
25
5
36
d
Error (%)
Maximum order L_{max}
Area
Volume
Reduced volume
Total mean curvature
0
5
10
15
20
25
30

Supplementary Figure 2 | SPHARM representation of a zebrafish embryo

(**a**) Maximum-intensity projection of a SiMView image stack showing a 22 hours post fertilization zebrafish embryo. Color indicates depth into the image. (**b**) SPHARM-MECH reconstructed surface of (a) with maximum order L_{max} = 20. (**c**) Reconstructed surfaces using increasing L_{max}. (**d**) Convergence of the spherical harmonics series (fidelity to the data): plot of percent error of surface properties of original surface mesh reconstruction *vs.* maximum order L_{max} used in fitting spherical harmonics coefficients. Scale bar, 100 μm.

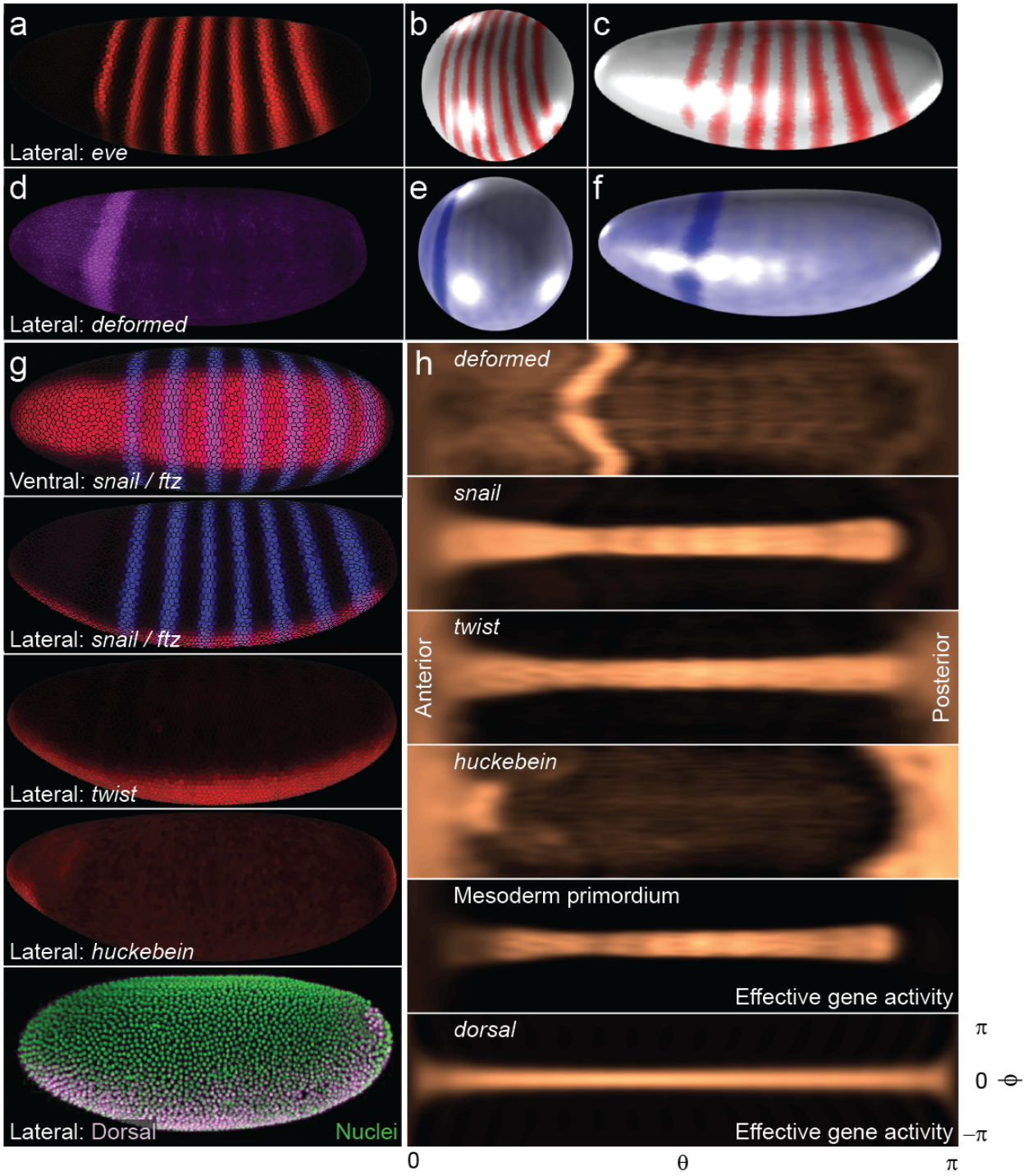
a
Lateral: eve
b
c
d
Lateral: deformed
e
f
g
Ventral: snail / ftz
Lateral: snail / ftz
Lateral: twist
Lateral: huckebein
Lateral: Dorsal
Nuclei
h
deformed
snail
twist
Anterior
Posterior
huckebein
Mesoderm primordium
Effective gene activity
dorsal
Effective gene activity
π
0
−π
ϕ
0
θ
π

Supplementary Figure 3 | Mapping of gene expression patterns and determination of mesoderm primordium and active regions

(**a**) Expression pattern of *eve*. (**b**) Mapping of *eve* to the unit sphere. (**c**) SPHARM-MECH representation of *eve* shown on the full blastoderm morphology. (**d-f**) same as a-c but for *deformed* (*dfd*) which is used to define the region of activity for the cephalic furrow formation. (**g**) From top to bottom: ventral and lateral views of *ftz* and *snail* patterns, lateral view *twist*, lateral view *huckebein* and lateral view *dorsal*. Data for *eve*, *dfd, snail*, *twist* and *huckebein* is obtained from the Berkeley Virtual Embryo Project and displayed using PointCloudXplore Light. (**h**) Two-dimensional angular plots of the spherical harmonics representation of *dfd*, *snail*, *twist* and *huckebein* (top four panels), the interaction map of *snail*, *twist* and *huckebein* (**Supplementary Note 8**), and (bottom most) the pattern of *dorsal*.

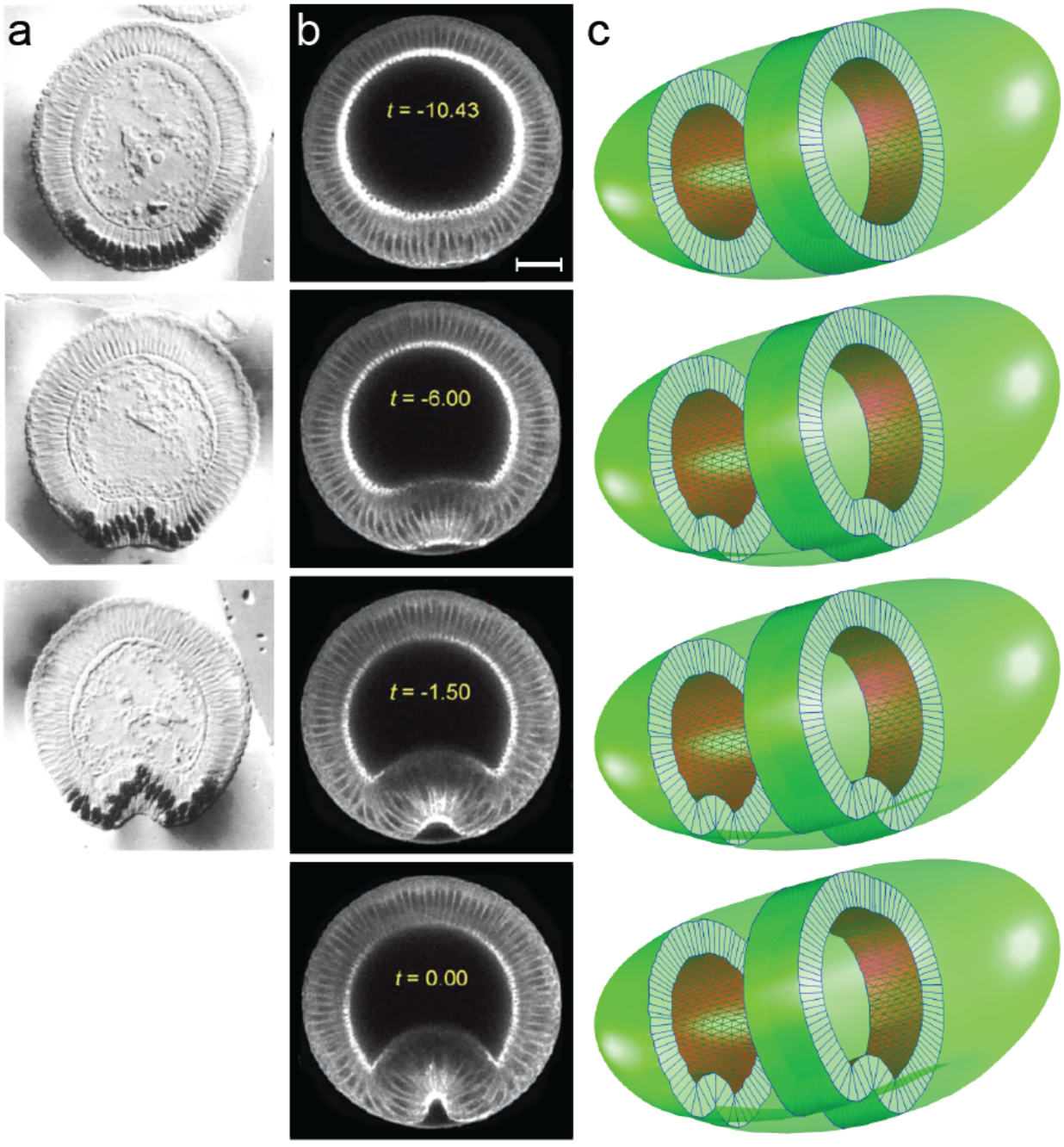
a
b
c
t = -10.43
t = -6.00
t = -1.50
t = 0.00

Supplementary Figure 4 | Ventral furrow invagination images compared to SPHARM-MECH simulation results

(**a**) *D. melanogaster* embryo electron microscopy images (adapted from Fig. 2 in Leptin and Grunewaldt [15]), and (**b**) multi-photon microscopy images of transgenic Sqh-GFP embryos (adapted from Fig. 6 in Conte *et al.* [20]). **(c)** SPHARM-MECH simulation of VFI showing a sequence of gradually increasing preferred curvatures when using the *dorsal*-based activity map of **Fig. 2a**. Scale bar, 20 μm.

a

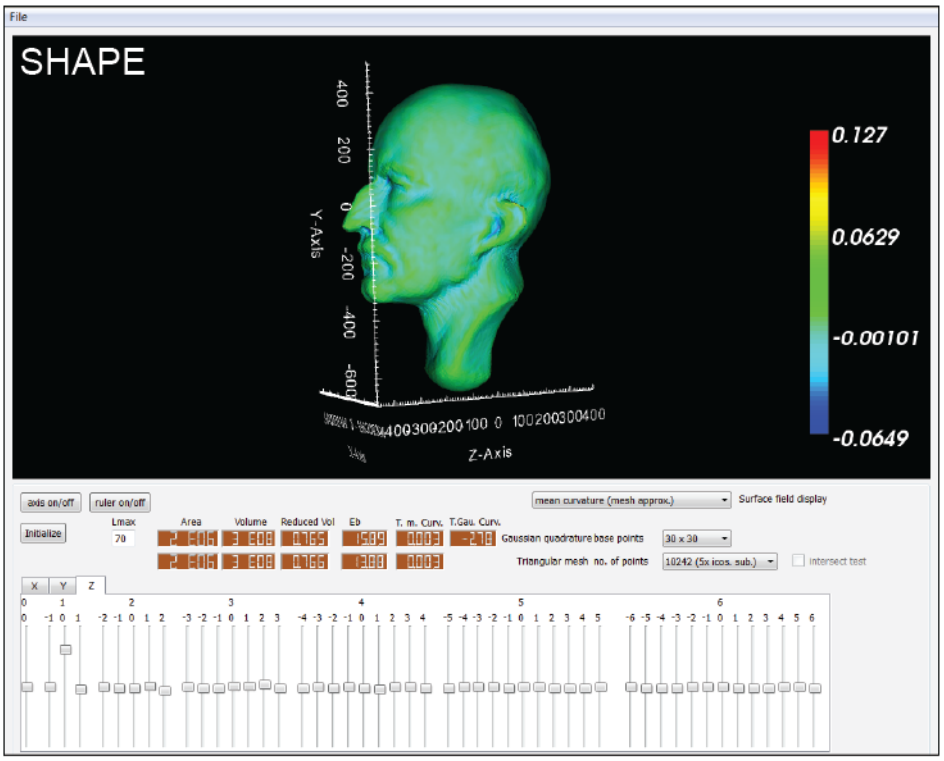
File
SHAPE
0.127
0.0629
-0.00101
-0.0649
Y-Axis
Z-Axis
axis on/off
ruler on/off
Initialize
Lmax
Area
Volume
Reduced Vol
Eb
T. m. Curv.
T.Gau. Curv.
mean curvature (mesh approx.)
Surface field display
Gaussian quadrature base points
Triangular mesh no. of points
intersect test

b

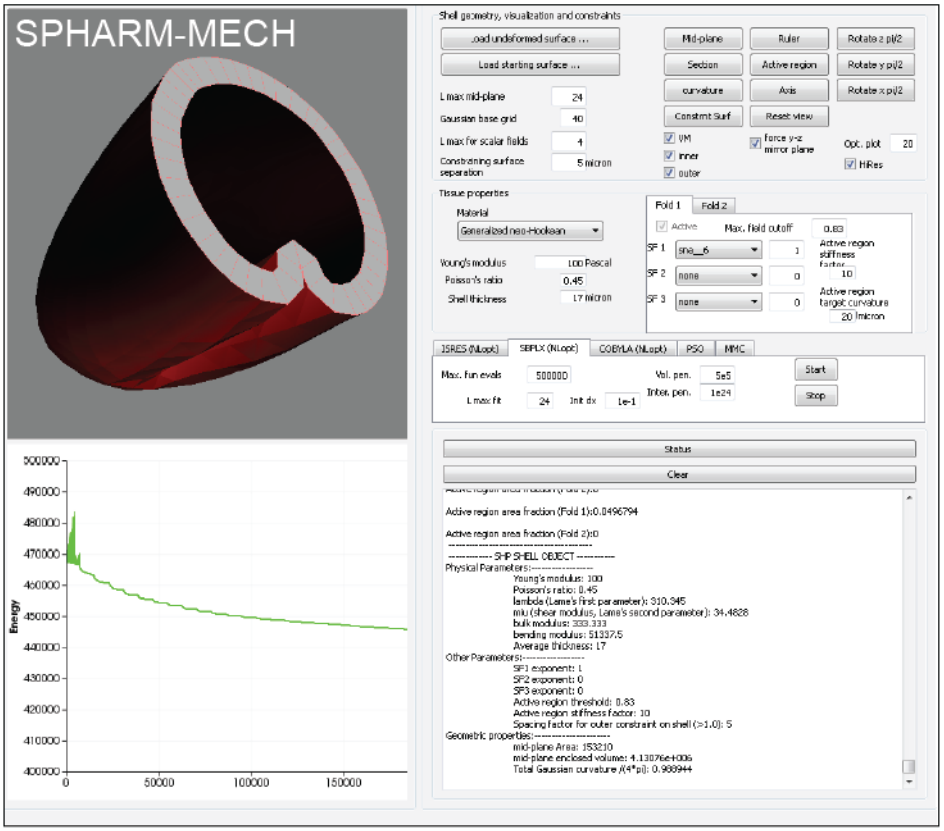
SPHARM-MECH
Shell geometry, visualization and constraints
Load undeformed surface ...
Load starting surface ...
Mid-plane
Ruler
Section
Active region
curvature
Axis
Constrnt Surf
Reset view
Tissue properties
Material
Generalized neo-Hookean
Young's modulus
Poisson's ratio
Shell thickness
Fold 1
Fold 2
Active region stiffness
Active region largest curvature
ISRES (NLopt)
SBPLX (NLopt)
COBYLA (NLopt)
PSO
MMC
Start
Stop
Status
Clear
Energy

Supplementary Figure 5 | Screenshots of SHAPE and SPHARM-MECH

(**a**) **SHAPE** (**S**pherical **HA**rmonic **P**arameterization **E**xplorer) is a MacOSX 64bit compiled program with a graphical user interface (GUI) that allows the user to view and modify SPHARM shapes that have been saved in the ".shp3" format. ".shp3" stores morphology and scalar fields such as gene expression patterns in the form of spherical harmonics coefficients in a text file. The program also demonstrates calculation of surface properties with Gaussian quadrature in comparison to usage of the triangular mesh. SHAPE is based on the shape_tools library and uses in addition QT and VTK (Visualization Toolkit) C++ libraries. (**b**) **SPHARM-MECH** (SPHARM-Mechanics) is a MacOSX 64bit compiled program with a GUI that allows the user to import shapes in the ".shp3" format, configure a tissue shell mechanics calculation and execute numerical optimization. The result is a lowest mechanical energy shape prediction. The screenshot shows a predicted VFI morphology at the end of an optimization using the SubPlex algorithm. SPHARM-MECH is based on the shape_tools library.

Supplementary Video 1 | SiMView time-lapse recording of fruit fly embryo undergoing gastrulation

The movie shows maximum-intensity projections of three dimensional stacks from a SiMView light-sheet microscopy time-lapse recording of a whole *D. melanogaster* embryo (2-min time intervals), homozygous for the membrane label Spider-GFP and the nuclear label His2Av-RFP, starting at the cellularized blastoderm stage. Each time point comprises two-color z-stacks recorded from four orthogonal optical views for two different physical orientations (dorso-ventral and lateral), encompassing the entire volume of the embryo with an axial step size of 1.95 µm. From left to right, the panels show the ventral half, first lateral half, dorsal half and second lateral half of the embryo.

Supplementary Video 2 | Control for physiological development after multi-color multi-angle SiMView time-lapse imaging

The movie shows maximum intensity projections of three dimensional stacks recoded with SiMView light-sheet microscopy (10-min time intervals), demonstrating normal development of the embryo and hatching of the intact larva. This long-term recording shows the same *D. melanogaster* embryo as in **Supplementary Video 1** and was started directly at the end of the

high-speed recording of gastrulation visualized in **Supplementary Video 1**. The movie provides a dorsal view of the multiview data set of the nuclear label His2Av-RFP, encompassing the entire volume of the embryo with an axial step size of 1.95 μm.

Supplementary Video 3 | Brief introduction to SHAPE

This video demonstrates the capabilities of SHAPE, to import/generate SPHARM objects, change the shapes interactively, calculate their geometrical properties, change their visualization, resolution and maximum spherical harmonic order, as well as exporting/saving shapes.

Supplementary Video 4 | Brief introduction to SPHARM-MECH (part 1)

This video demonstrates the main steps required to import data into SPHARM-MECH, manipulate the view and inspect the gene expression pattern list.

Supplementary Video 5 | Brief introduction to SPHARM-MECH (part 2)

This video introduces the SPHARM-MECH GUI.

Supplementary Video 6 | Brief introduction to SPHARM-MECH (part 3)

This video demonstrates the configuration of a basic SPHARM-MECH simulation.

References

1. Heiskanen, W.A. & Moritz, H. Physical Geodesy. (Freeman and Company, San Francisco; 1967).
2. Bosh, W. On the computation of Derivatives of Legendre Functions. *Physics and chemistry of the earth* **25**, 655-659 (2000).
3. Hobson, E.W. The theory of spherical and ellipsoidal harmonics. (Chelsea, New York; 1955).
4. Kautzleben, H. Kugelfunktionen. (Teubner, Leipzig; 1965).
5. O'Neill, B. Elementary Differential Geometery. (Academic Press, San Diego; 1997).
6. Davis, P. & Rabinowitz, P. Methods of Numerical Integration. (Academic Press, New York; 1975).
7. Carr, J.C., Fright, W.R. & Beatson, R.K. Surface Interpolation with Radial Basis Functions for Medical Imaging. *IEEE Trans Med Imaging* **16**, 96-107 (1997).
8. Treece, G.M., Prager, R.W. & Gee, A.H. Regularized marching tetrahedra: improved iso-surface extraction. *Computers and Graphics* **23**, 583-598 (1999).
9. Khairy, K. & Howard, J. Spherical Harmonics-Based Parametric Deconvolution of 3D Surface Images using Bending Energy Minimization. *Med Image Anal* **12**, 217-227 (2008).
10. Press, W.H., Teukolsky, S.A., Vetterling, W.T. & Flannery, B.P. Numerical Recipes in C. (Cambridge University Press, 1992).
11. Bower, A.F. Applied mechanics of solids. (CRC Press, 2009).
12. Timoshenko, S. & Woinowsky-Krieger, S. The Theory of Plates and Shells, Edn. 2. (Mcgraw-Hill Higher Education, 1964).
13. Brechbühler, C., Gerig, G. & Kuebler, O. Parametrization of closed surfaces for 3-D shape description. *Comput Vision Image Und* **61**, 154-170 (1995).
14. Sweeton, D., Parks, S., Costa, M. & Wieschaus, E. Gastrulation in Drosophila: the formation of the ventral furrow and posterior midgut invaginations. *Development* **112**, 775-789 (1991).
15. Leptin, M. & Grunewald, B. Cell shape changes during gastrulation in Drosophila. *Development* **110**, 73-84 (1990).
16. Fowlkes, C.C. et al. A quantitative spatiotemporal atlas of gene expression in the Drosophila blastoderm. *Cell* **133**, 364-374 (2008).
17. Markow, T.A., Beall, S. & Matzkin, L.M. Egg size, embryonic development time and ovoviviparity in Drosophila species. *J Evol Biol* **22**, 430-434 (2009).
18. Tomer, R., Khairy, K., Amat, F. & Keller, P.J. Quantitative high-speed imaging of entire developing embryos with simultaneous multiview light-sheet microscopy. *Nat Methods* **9**, 755-763 (2012).
19. Royer, L.A. et al. Adaptive light-sheet microscopy for long-term, high-resolution imaging in living organisms. *Nat Biotechnol* **34**, 1267-1278 (2016).
20. Conte, V. et al. A biomechanical analysis of ventral furrow formation in the Drosophila melanogaster embryo. *PLoS One* **7**, e34473 (2012).